Monthly Notices of the ROYAL ASTRONOMICAL SOCIETY

MNRAS **454,** 3002–3019 (2015) doi:10.1093/mnras/stv2138

Secondary eclipse observations for seven hot-Jupiters from the Anglo-Australian Telescope

G. Zhou,[1,2★] D. D. R. Bayliss,[1,3] L. Kedziora-Chudczer,[4,5] C. G. Tinney,[4,5] J. Bailey,[4,5] G. Salter[6] and J. Rodriguez[7]

[1]*Research School of Astronomy and Astrophysics, Australian National University, Canberra, ACT 2611, Australia*
[2]*Harvard-Smithsonian Center for Astrophysics, 60 Garden St, Cambridge, MA 02138, USA*
[3]*Observatoire Astronomique de l'Université de Genève, 51 ch. des Maillettes, CH-1290 Versoix, Switzerland*
[4]*Australian Centre for Astrobiology, University of New South Wales, Sydney, NSW 2052, Australia*
[5]*Australian Centre for Astrobiology, University of New South Wales, Sydney, NSW 2052, Australia*
[6]*Laboratoire d'astrophysique de Marseille, Technople de Marseille-Etoile 38, rue Frdric Joliot-Curie, F-13388 Marseille cedex 13, France*
[7]*Department of Physics and Astronomy, Vanderbilt University, 6301 Stevenson Center, Nashville, TN 37235, USA*

Accepted 2015 September 14. Received 2015 September 11; in original form 2015 May 7

ABSTRACT

We report detections and constraints for the near-infrared *K*s band secondary eclipses of seven hot-Jupiters using the IRIS2 infrared camera on the Anglo-Australian Telescope. Eclipses in the *K*s band for WASP-18b and WASP-36b have been measured for the first time. We also present new measurements for the eclipses of WASP-4b, WASP-5b, and WASP-46b, as well as upper limits for the eclipse depths of WASP-2b and WASP-76b. In particular, two full eclipses of WASP-46b were observed, allowing us to demonstrate the repeatability of our observations via independent analyses on each eclipse. Significant numbers of eclipse depths for hot-Jupiters have now been measured in both *K*s and the four *Spitzer* IRAC bandpasses. We discuss these measurements in the context of the broad-band colours and brightness temperatures of the hot-Jupiter atmosphere distribution. Specifically, we re-examine the proposed temperature dichotomy between the most irradiated, and mildly irradiated planets. We find no evidence for multiple clusters in the brightness temperature–equilibrium temperature distributions in any of these bandpasses, suggesting a continuous distribution of heat re-emission and circulation characteristics for these planets.

Key words: occultations – planets and satellites: atmospheres.

1 INTRODUCTION

A secondary eclipse occurs when the emergent flux from a planet is blocked by its host star, which allows the direct measurement of the infrared day side temperature of a hot-Jupiter. Assembling a sample of secondary eclipses is one way to comparatively study the atmospheres of the hot-Jupiter population. For example, Cowan & Agol (2011) have compared measured effective temperatures to the incident stellar irradiation received by hot-Jupiters, and proposed that the most irradiated planets have heat re-emission properties that are different from those for cooler planets. Updated results from Schwartz & Cowan (2015) have constructed ensemble emission spectra of the hot-Jupiter population, and placed further constraints on the albedo and heat recirculation efficiencies of the most well characterized hot-Jupiters. Triaud (2014) and Triaud et al. (2014) have used multiband eclipse measurements to create colour–magnitudes diagrams of hot-Jupiters, enabling an empirical comparison with the broad-band spectral features of M-dwarfs and brown dwarfs. The presence of proposed atmospheric thermal inversion features have also been linked to stellar activity (Knutson, Howard & Isaacson 2010) via comparative studies.

The majority of secondary eclipse measurements have been made using the *Spitzer Space Telescope* in the IRAC bands (e.g. Deming et al. 2015; Lanotte et al. 2014; Shporer et al. 2014). 48 planets have now been sampled in eclipse at the IRAC 4.5 μm band. In comparison, only 26 planets have been observed in the *K*s band from the ground. However, ground-based eclipse observations can probe shorter wavelengths that are inaccessible to *Spitzer*, and so probe deeper into the planetary atmosphere and examine different regimes of atmospheric circulation. They also provide an extended wavelength baseline for comparison with spectral models. Despite the challenges inherent in ground-based eclipse measurements for hot-Jupiters, a number of facilities are now consistently delivering eclipse depth measurements. These include the Canada–France–Hawaii Telescope (Croll et al. 2010a,b,2011, 2015; Wang et al. 2013), 200-inch at Palomar (e.g. Zhao et al. 2012a,b, 2014; O'Rourke et al. 2014; Shporer et al. 2014), and the European

★ E-mail: george.zhou@cfa.harvard.edu

Table 1. Targets and observation details.

Target	*K* mag[a]	Observation date & time (UT)[b]	Number of exposures	Cadence (s)	Median FWHM (pix)	No. ref stars
WASP-2	9.6	2014-09-10 08:54–14:46	3100	6	7.6	9
WASP-4	10.7	2014-09-04 15:54–17:02	354	11	17.4	4
		2014-09-11 09:23–11:38	689	11	14.2	4
WASP-5	10.6	2014-09-14 13:17–19:17	1727	11	12.3	6
WASP-18	8.1	2014-09-05 11:16–14:54	95	120[c]	19.0	3
WASP-36	11.3	2015-03-09 10:21–15:51	4358	4	4.1	9
WASP-46	11.4	2014-09-11 12:07–17:28	1600	11	13.4	6
		2014-09-14 08:55–12:53	1230	11	11.6	6
WASP-76	8.2	2014-09-13 13:26–19:16	2953	6	17.4	2

Notes. [a]2MASS magnitudes (Skrutskie et al. 2006).
[b]Start and end of each observation sequence.
[c]20 × 5 s exposures are averaged and used for analysis. Individual exposures were not saved.

Southern Observatory (ESO) 2.2-m telescope (e.g. Chen et al. 2014a,b,c).

In Zhou et al. (2014), we introduced the series of eclipse observations we are performing at the Anglo-Australian Telescope (AAT), with the aim of measuring *K*s band eclipses for a large number of hot-Jupiters in the Southern hemisphere. In this paper, we report eclipse measurements and constraints for seven hot-Jupiters: WASP−2b, −4b, −5b, −18b, −36b, −46b, and −76b. The observations and analysis are described in Section 2, results and comparisons between previous observations reported in Section 3. Section 4 discusses the eclipse observations in the context of the hot-Jupiter colour–magnitude, colour–colour diagrams, and brightness temperature–equilibrium temperature relationships.

2 OBSERVATIONS AND ANALYSIS

2.1 Observing strategy and data reduction

These eclipse observations were performed using the IRIS2 instrument (Tinney et al. 2004) on the 3.9-m AAT at Siding Spring Observatory, Australia. IRIS2 is a 1 K × 1 K infrared camera with a HAWAII-1 HgCdTe infrared detector, read out over four quadrants in double-read mode. The instrument has a field of view of 7.7 arcmin × 7.7 arcmin and plate scale of 0.4486 arcsec pixel^{-1}. The observing strategy for each eclipse observation is similar to that described in Zhou et al. (2014): the telescope is defocused to broaden the stellar point spread function, reducing the effect of intra- and interpixel systematics, and preventing saturation of the target and key reference stars. Exposure times are set such that the target and key reference stars are kept below peak counts of 20 000 ADU, so as to keep within the regime where detector non-linearity is minimized (non-linearity of >1 per cent occurs above 40 000 ADU). We apply a non-linearity correction to each image, following the IRIS2 manual's prescription, to correct the very small (<0.05 per cent) non-linearity present below 20 000 ADU. Typical exposure times are <10 s per exposure. The WASP-18 observations were taken using 5 s exposures, with 20 exposures being averaged and saved as a single frame. This observing mode was tested to reduce the data volume of the observations. However, we found that it led to a reduction in the precision of eclipse timing and depth measurements, and it was not used for any subsequent observations. For all other observations, single exposures are saved and used in the analysis. Observations of six offset positions are taken before and after each eclipse sequence to sample the sky background. These observations are used as flat-fields in the reduction process. The field is carefully centred such that the target and key reference stars do not fall on bad pixels. The eclipse sequence is performed in stare mode, with the telescope guided to minimize drift of the field. Dark frames of the same exposure time as the eclipse observations are taken before and after each night. Tests of darks taken through an experimental night showed no drifts in the dark current. Information on the systems observed, and the specifics of each eclipse observation, including date, number of exposures, median cadence, median point spread function, full width at half-maximum (FWHM), are given in Table 1.

Each object frame is dark subtracted and flat divided. A master dark frame is median combined from darks of the same exposure time, taken on the same night as the object frames. Master flat-fields are created from the set of offset frames taken before and after the eclipse sequence, with stars masked, and median combined. Bad pixels in the object frames are then interpolated over using the surrounding pixels via a radial basis function interpolation. Barycentric Julian Date (BJD) time stamps for each frame are calculated using the convert time task in VARTOOLS (Hartman et al. 2008; Eastman, Siverd & Gaudi 2010).

For each frame, stars are identified using Source Extractor (Bertin & Arnouts 1996) and cross matched using *grmatch* task in FITSH (Pál 2012). Coordinates for the target and reference stars are transformed using GRTRANS, and aperture photometry performed using FIPHOT. For each set of observations, we extract the photometry through a set of fixed apertures. Background flux beneath each aperture is measured in a 5-pixel wide annulus around each central aperture. Adjacent stars within this annular background aperture are masked before the background is calculated. We also tried extractions using variable apertures, by setting the aperture size per frame as a multiple of the average FWHM of the stellar point spread functions. However, extracting photometry using fixed apertures yielded light curves with the least out-of-eclipse scatter. We conclude photometry using variable aperture sizes introduces noise associated with the FWHM estimate, and especially for fields with just a few bright reference stars.

2.2 Light-curve analysis and modelling

The object light curve is corrected by a master reference light curve, constructed from selected reference stars. Weights are applied to each reference star light curve such that the out-of-eclipse scatter of the object light curve is minimized after correction. The final light curve is found by minimizing the out-of-transit scatter of the

Table 2. Model fit and derived eclipse parameters.

Model priors[a]						Model fit parameters			Derived parameters	
Planet	Period (days)	T_0 (BJD–TDB)[b]	$(R_p + R_*)/a$	R_p/R_*	i (°)	$e\cos\omega$	S_p/S_*	Detrending parameters[c]	F_p/F_* Eclipse depth (%)	T_B (K)
WASP-2b	2.152 2214 ±0.000 0004	2453991.5153 ±0.0002	0.140 ± 0.002	0.1326 ± 0.0007	84.8 ± 0.2	$-0.001^{+0.001}_{-0.001}$[d]	<0.042	*A*, *t*, *Y*	<0.07	<1900
WASP-4b	1.338 2320 ±0.000 0002	2454823.59192 ±0.000 03	0.211 ± 0.001	0.1545 ± 0.0003	88.5 ± 0.4	$-0.001^{+0.003}_{-0.003}$	$0.07^{+0.02}_{-0.02}$	2014-09-04: *t* 2014-09-11 *t*, *X*	$0.16^{+0.04}_{-0.04}$	1900^{+100}_{-100}
WASP-5b	1.628 425 ±0.000 001	2454375.6257 ±0.0002	0.203 ± 0.007	0.111 ± 0.001	86 ± 1	$0.008^{+0.002}_{-0.002}$	$0.16^{+0.02}_{-0.02}$	*A*, *t*	$0.20^{+0.02}_{-0.02}$	2500^{+100}_{-100}
WASP-18b	0.941 4518 ±0.000 0004	2455084.79283 ±0.00009	0.306 ± 0.009	0.097 ± 0.001	85 ± 2	$0.012^{+0.007}_{-0.008}$	$0.14^{+0.03}_{-0.03}$	*t*	$0.13^{+0.03}_{-0.03}$	2500^{+200}_{-200}
WASP-36b	1.537 365 ±0.000 003	2455569.8381 ±0.0001	0.190 ± 0.003	0.1384 ± 0.007	83.6 ± 0.2	$0.004^{+0.006}_{-0.005}$	$0.07^{+0.02}_{-0.02}$	*A*, *t*, *Y*	$0.13^{+0.04}_{-0.04}$	1900^{+100}_{-200}
WASP-46b	1.430 370 ±0.000 002	2455392.3163 ±0.0002	0.200 ± 0.006	0.147 ± 0.007	82.6 ± 0.4	$0.004^{+0.002}_{-0.002}$	$0.12^{+0.02}_{-0.02}$	2014-09-11: *A*, *t* 2014-09-14: *A*, *t*, *F*	$0.26^{+0.05}_{-0.03}$	2200^{+100}_{-100}
WASP-76b	1.809 886 ±0.000 001	2456107.8551 ±0.0003	0.270 ± 0.007	0.1090 ± 0.0007	88 ± 2	$-0.001^{+0.004}_{-0.004}$[e]	<0.26	*A*, *F*, *t*, *Y*	<0.3	<3500

Notes. [a]Priors adopted from literature system parameters: WASP-2b (Collier Cameron et al. 2007; Southworth et al. 2010), WASP-4b (Wilson et al. 2008; Hoyer et al. 2013), WASP-5b (Anderson et al. 2008; Southworth et al. 2009a), WASP-18b (Hellier et al. 2009; Southworth et al. 2009b), WASP-36b (Smith et al. 2012a), WASP-46b (Anderson et al. 2012), WASP-76b (West et al. 2013).
[b]Where appropriate, transit times reported in HJD–UTC have been translated to BJD–TDB using Eastman et al. (2010).
[c]The set of detrending parameters are airmass *A*, background flux *B*, FWHM *F*, linear time dependent trend *t*, target X pixel positions *X* and *Y*.
[d]$e\cos\omega$ for WASP-2b constrained by Gaussian prior from *Spitzer* eclipse measurements to be -0.0013 ± 0.0009 (Wheatley et al. 2010).
[e]$e\cos\omega$ for WASP-76b constrained by Gaussian prior from radial velocity measurements to be 0.00 ± 0.02 (West et al. 2013).

object light curve for all permutations of object and reference star extraction apertures.

The eclipse light curves are fitted with the Nelson & Davis (1972) model, using an adapted implementation of the JKTEBOP code (Popper & Etzel 1981; Southworth, Maxted & Smalley 2004). The eclipses are modelled with free parameters $e\cos\omega$, which determines the phase of the eclipse, and the surface brightness ratio S_p/S_*, which determines the depth of the eclipse. To propagate the uncertainties in the system parameters, we also incorporate the free parameters period P, primary transit reference time T_0, planet–star radius ratio R_p/R_*, normalized orbit radius $(R_p + R_*)/a$, and line-of-sight inclination i, each constrained tightly by Gaussian priors adapted from the literature uncertainties. In the cases where no clear eclipse is seen, we constrain the $e\cos\omega$ with Gaussian priors using literature eccentricity values from previous *Spitzer* eclipse measurements, or radial velocity constraints. The $e\cos\omega$ constraints, when applied, are noted in Table 2. The light travel time has been accounted for when fitting for the eclipse timing.

To incorporate the influence of instrumental and atmospheric variations into the reported uncertainties, we model the light curve as a function of external parameters simultaneously with the model fit. This is even more important for infrared light curves than at optical wavelengths, given the greater pixel-to-pixel sensitivity variations in infrared detectors, combined with the much larger variability of the infrared sky background. The influence of the external parameters is modelled as a linear combination of factors which include (as per Zhou et al. 2014): time t, target star pixel positions X and Y, stellar point spread functions FWHM F, background counts B, and airmass A. Fits are performed using all combinations of the external parameters. We then adopt the model with the set of external parameters that minimize the Bayesian Information Criterion (BIC) post-fitting. The external parameter model components adopted for each eclipse observation are listed in Table 2. We note in Section 3 when the next-best decorrelation models, ranked by BIC, exhibit a different eclipse fit. In the cases where eclipse observations are combined from multiple nights (WASP-4b and WASP-46b), the external parameters and coefficients are independent for each night. This allows us to account for the different factors that affect the observations each time. For example, the seeing conditions were stable for the WASP-46b observation on 2014-09-11, and variable for 2014-09-14, the instrument model thus contained only the time and airmass components for the first night, and time, airmass, and FWHM components for the second.

The best-fitting model parameters and associated uncertainties are derived using an Markov chain Monte Carlo (MCMC) analysis, via the EMCEE ensemble sampler (Foreman-Mackey et al. 2013). The MCMC analyses are run twice, with the walkers for the second run originating from the best-fitting parameters from the first run. In the second run, the per-point photon errors are inflated to force a reduced $\chi^2 = 1$. This allows error sources other than photon noise to be included in the uncertainty estimate, and is particularly important for light curves with substantial red noise components.

3 RESULTS

We detect the eclipses of WASP-4b, -5b, -18b, -36b, and -46b at $>3\sigma$ significance, and provide the 3σ upper limits for the eclipses of WASP-2b and -76b. The full set of derived parameters, including flux ratios, eccentricity constraints, and brightness temperatures, are listed in Table 2. The light curves for the eclipse observations are plotted in Figs 1–7, with the 3σ upper limits marked where appropriate.

For WASP-2b, we determine a 3σ upper limit to the eclipse depth of <0.07 per cent from a single eclipse observation. The eclipse of WASP-2b has previously been measured with *Spitzer* (Wheatley et al. 2010) at 3.6, 4.5, 5.9, and 8.0 μm. Given the lower flux ratio expected in the *Ks* band compared to the *Spitzer* bands, and the shallow 0.083 ± 0.035 per cent eclipse at 3.6 μm, our upper limit is consistent with the previous observations. The eclipse phase in our model fit was constrained by a Gaussian prior centred on the *Spitzer* eclipse detection. The AAT-IRIS2 light curve for the eclipse event of WASP-2b is plotted in Fig. 1.

For WASP-4b, we use two partial eclipses to determine an eclipse depth of $0.16^{+0.04}_{-0.04}$ per cent, and phase consistent with circular orbit of $e\cos\omega = -0.001^{+0.003}_{-0.003}$. The *Ks* band eclipse has been previously

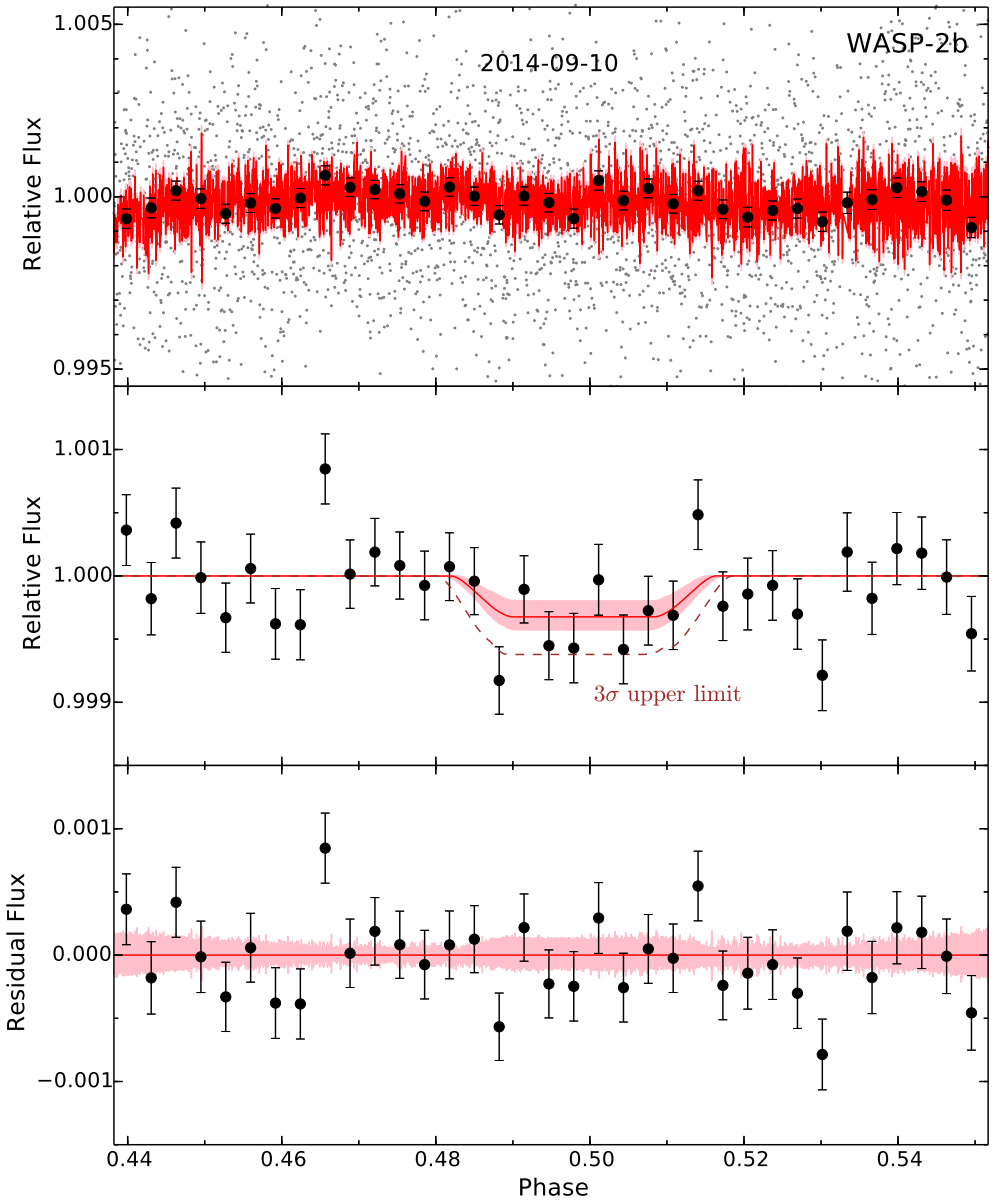

Figure 1. Top: the *K*s band relative photometry light curve for the eclipse event of WASP-2b as measured on 2014-09-10. Photometry from individual observations are plotted in grey, 10 min bins in black. For each bin containing n points, the error bars are plotted to represent the mean per-point uncertainties, which are photon errors inflated to force a reduced $\chi^2 = 1$, scaled by $1/\sqrt{n}$. The best-fitting model (eclipse and instrumental parameters) is plotted in red, and 68 per cent of the allowed models reside within the shaded pink region. Middle: as above, but with only the 10 min binned data and the instrument model subtracted. The shaded regions show the allowed models in terms of the transit parameters only. Since we can only place an upper limit on the eclipse of WASP-2b, the dashed brown line represents the 3σ regime of the models. Bottom: as above, but showing the data residuals to the best-fitting model. The shaded region shows the difference between each allowed model (eclipse and instrumental) to the best-fitting model.

measured by Cáceres et al. (2011), using ISAAC on the very large telescope, at a depth of $0.185^{+0.014}_{-0.013}$ per cent, consistent with our measurement to within 1σ. The eclipses were also measured by *Spitzer* at 3.6 and 4.5 μm (Beerer et al. 2011). The eclipse phase we measure is also consistent to 1σ with that measured by Cáceres et al. (2011) and Beerer et al. (2011). The AAT-IRIS2 light curves for the eclipse events of WASP-4b are plotted in Fig. 2.

For WASP-5b, we observe an eclipse with a depth of $0.20^{+0.02}_{-0.02}$ per cent, and an eccentricity estimate from the eclipse phase of $e\cos\omega = 0.008^{+0.002}_{-0.002}$. A *K*s band eclipse depth of $0.269^{+0.062}_{-0.062}$ per cent was measured by Chen et al. (2014b) using GROND on the MPG 2.2 m telescope. The eclipse has also been measured in the *J* band (Chen et al. 2014b), and at the 3.6 and 4.5 μm *Spitzer* bands (Baskin et al. 2013). Our $e\cos\omega$ measurement indicates the orbit is eccentric with a statistical significance of 4σ, and is consistent within 1σ with Chen et al. (2014b), and within 2σ with Baskin et al. (2013). WASP-5b has a short period, leading to a short tidal circularization time-scale. Following equation 1 of Dobbs-Dixon, Lin & Mardling (2004), the tidal circularization time-scale should be ∼1 Myr (assuming a tidal quality factor of $Q' = 10^5$). It is interesting that the eccentricity is non-zero, suggesting that perhaps a larger tidal quality factor is required to describe the system. The AAT-IRIS2 light curve for the eclipse event of WASP-5b is plotted in Fig. 3.

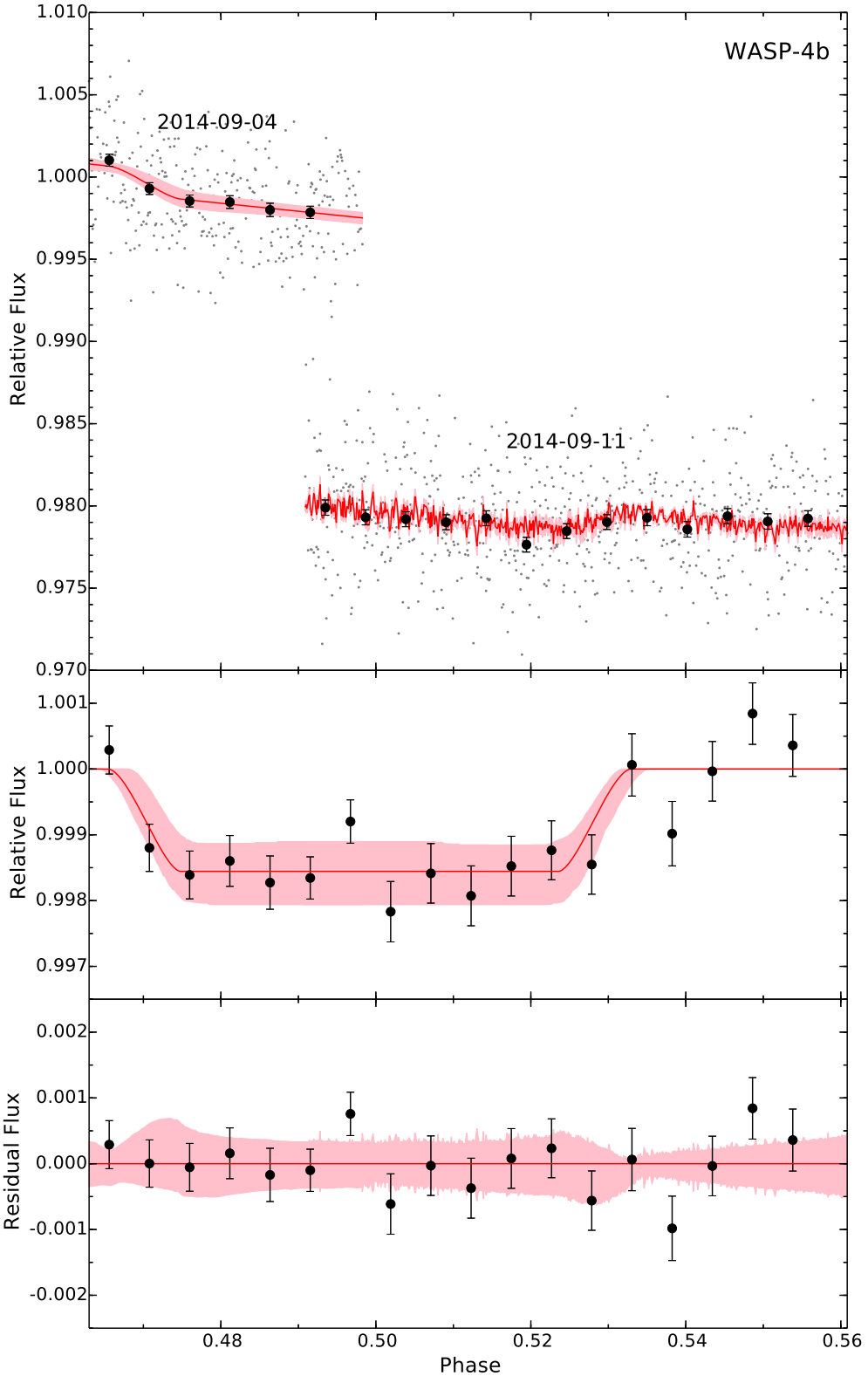

Figure 2. Light curves for the eclipse events of WASP-4b as observed on 2014-09-04 and 2014-09-11, labelled as per Fig. 1, but with the light curves from each night arbitrary offset for clarity in the top panel.

For WASP-18b, we measure an eclipse depth of $0.14^{+0.03}_{-0.03}$ per cent, and an eccentricity estimate from the eclipse phase of $e\cos\omega = 0.012^{+0.007}_{-0.008}$. The eclipses have previously been measured by *Spitzer* at 3.6 and 4.5 μm by Nymeyer et al. (2011) and Maxted et al. (2013), and at 5.9 and 8.0 μm by Nymeyer et al. (2011). The eclipse phase we derive is consistent (at the 2σ level) with that expected from circular orbit, and the measurements from the *Spitzer* observations. The long cadence

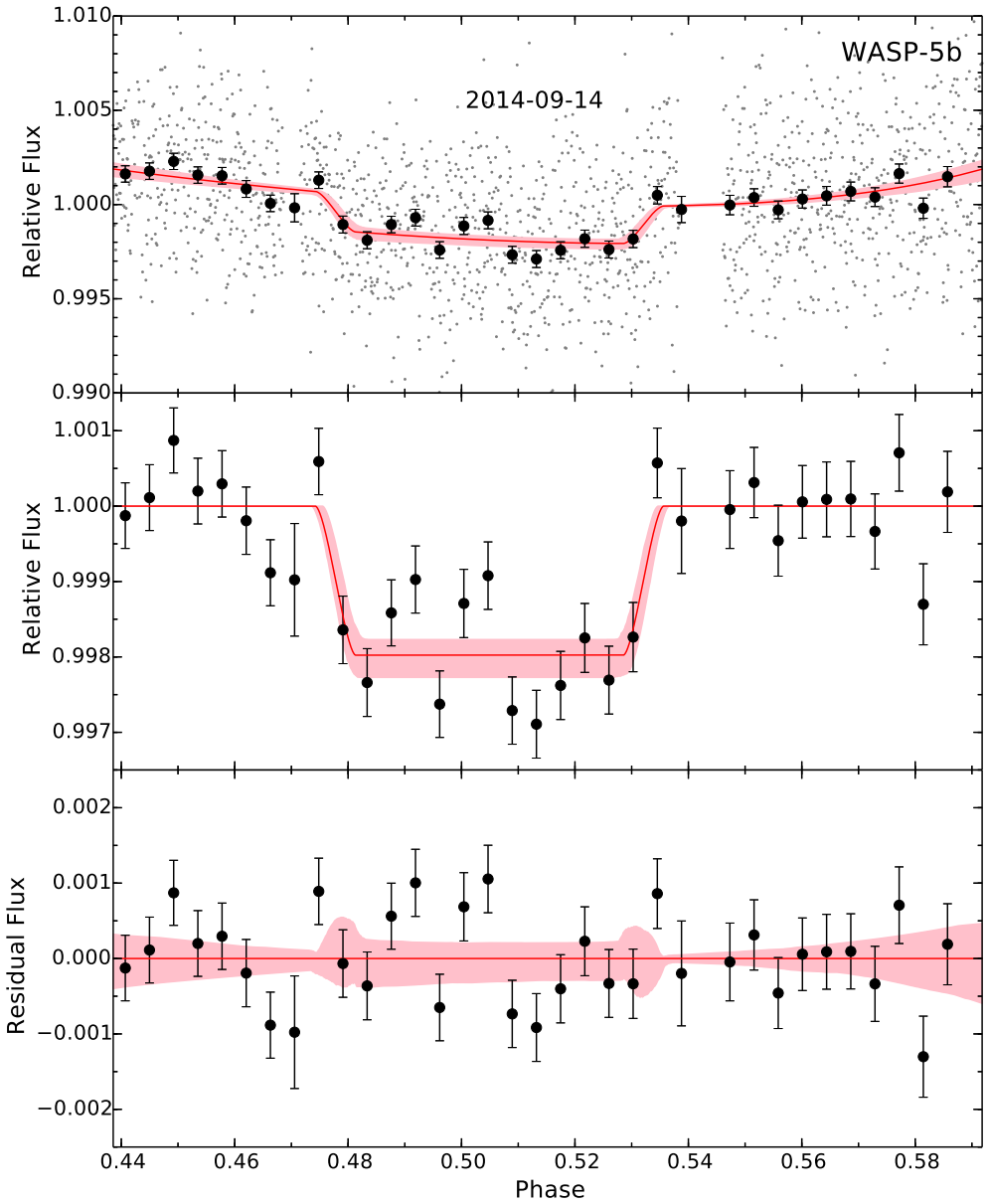

Figure 3. Light curve for the eclipse event of WASP-5b, plotted as per the description for Fig. 1.

observing strategy used for the WASP-18b observations results in a larger uncertainty in eclipse phase than for other targets. We also caution that the second-best model, ranked by Δ BIC (with Δ BIC of 4), involves the time and background flux terms, reducing the surface flux ratio to $S_p/S_\star = 0.10^{+0.07}_{-0.06}$. The third-best detrending model involves the detector y-position, and gave an eclipse depth consistent with that of the best-fitting model. The AAT-IRIS2 light curve for the eclipse event of WASP-18b is plotted in Fig. 4.

For WASP-36b, we report the first eclipse detection of the system at depth of $0.13^{+0.04}_{-0.04}$ per cent, and eccentricity of $0.004^{+0.006}_{-0.005}$, consistent with a circular orbit. No previous eclipse observations have been reported for this planet. The AAT-IRIS2 light curve for the eclipse event of WASP-36b is plotted in Fig. 5.

For WASP-46b, we measure an eclipse depth of $0.26^{+0.05}_{-0.03}$ per cent, and $e\cos\omega = 0.004^{+0.004}_{-0.004}$, as measured from two full eclipse observations. The Ks band eclipse has previously been measured by Chen et al. (2014c), with a reported depth of $0.253^{+0.063}_{-0.060}$ per cent, consistent with our measurement to better than 1σ. Chen et al. (2014c) also measured the J- and H-band eclipses using GROND on the ESO 2.2 m. The eclipse timing is also consistent with that of a circular orbit, and that reported by Chen et al. (2014c) to 1σ. The AAT-IRIS2 light curves for the eclipse events of WASP-46b are plotted in Fig. 6.

For WASP-76b, we find a 3σ upper limit eclipse depth of 0.3 per cent, with a marginal detection at 2.3σ of a $0.13^{+0.06}_{-0.06}$ per cent eclipse. The eclipse phase fit was constrained by a Gaussian prior on the orbit eccentricity (West et al. 2013). The marginal eclipse detection is not well constrained in eclipse phase due to the lack of sufficient pre-ingress baseline. As a result, the 3σ upper limit is asymmetric about the eclipse centre. No previous eclipse observations have been reported for this planet. The AAT-IRIS2 light curve for the eclipse event of WASP-76b is plotted in Fig. 7.

For each set of eclipses, we also calculate a β factor to check for any residual time-correlated noise to the light curves (Winn et al.

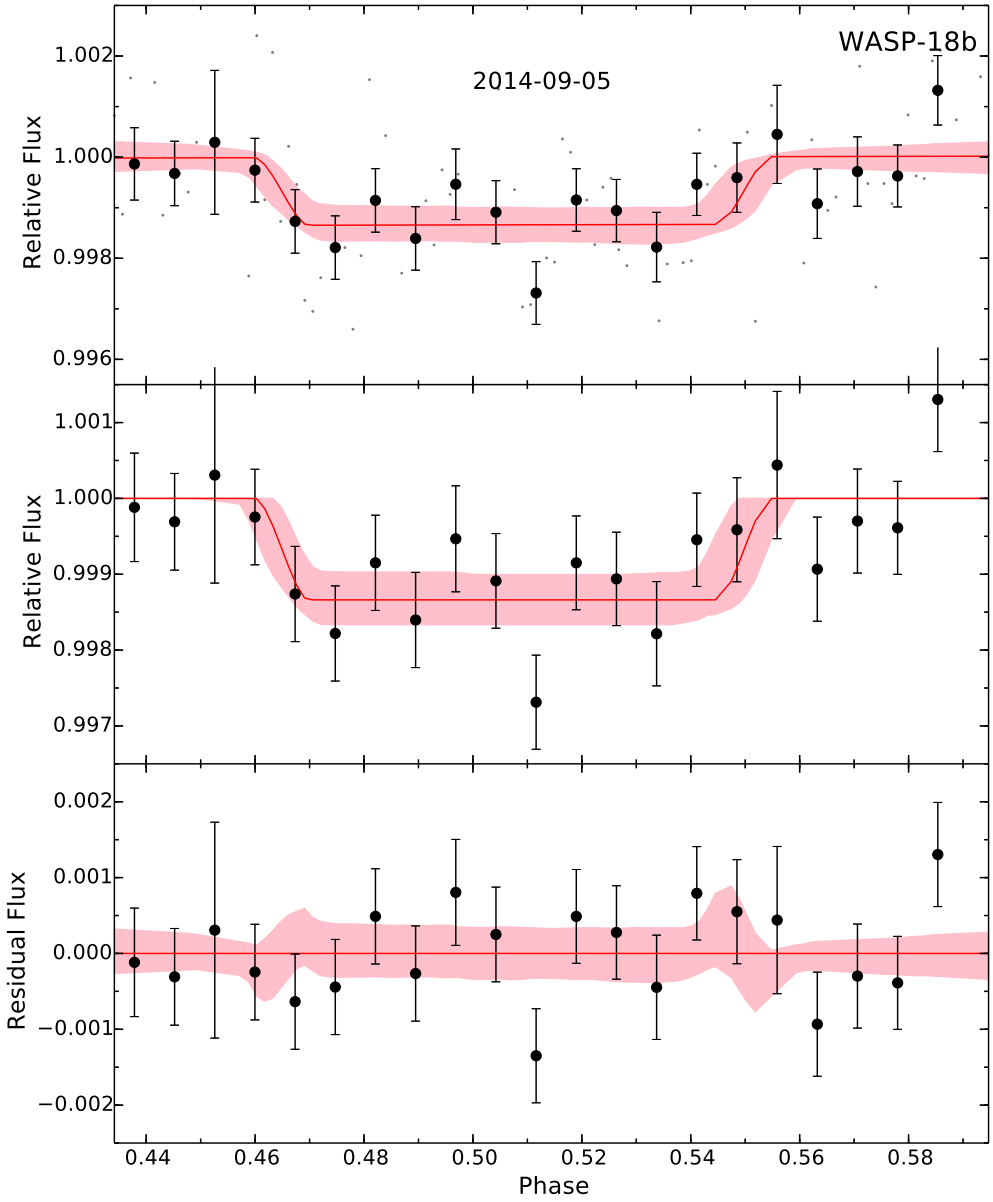

Figure 4. Light curve for the eclipse event of WASP-18b, plotted as per the description for Fig. 1.

2008). We compared the progressive binned scatter of the light-curve residual (i.e. the data with the eclipse and external parameter models subtracted) with the expected scatter assuming only photon noise. For every m bins of n points, we measure a root mean square (rms) scatter σ_n, which is then compared to the expected photon noise scaled rms from the unbinned light curve (σ_1), according to

$$\sigma_n = \beta \frac{\sigma_1}{\sqrt{n}} \sqrt{\frac{m}{m-1}}. \quad (1)$$

For light curves with no time-correlated noise, $\beta = 1$. The average β value for each light curve, calculated for bins between 60 and 600 s, along with the rms–bin size relationships, are shown in Fig. 8.

4 DISCUSSION

We report new *Ks* band eclipse depth measurements and constraints for seven hot-Jupiters. These results bring the total number of planets with eclipses monitored at 2.1 μm to 25, a sample large enough to allow some initial statistical insight into the atmospheres of the hot-Jupiter population.

Such statistical analyses require a set of robust measurements with reliable uncertainty estimates. To characterize the robustness and repeatability of our measurements, we performed an independent analysis for the two full eclipses of WASP-46b that we obtained (Fig. 6). We derived self-consistent eclipse phases and depths between the two eclipses to within 1σ ($e \cos\omega$ of $0.006^{+0.005}_{-0.005}$ and $0.001^{+0.004}_{-0.004}$, and eclipse depth F_p/F_* of $0.25^{+0.05}_{-0.05}$ and $0.32^{+0.06}_{-0.05}$ per cent). On both nights, the eclipses were detected at $>5\sigma$ significance, and the measured eclipse parameters were consistent with each other at the 1σ level. Literature *Ks* band eclipse measurements also exist for WASP-4b, -5b, and -46b. The eclipse depths we report are also consistent within 1σ to all the previous measurements. This increases our confidence of the uncertainty measurements presented by the series of ground-based eclipse observations to date. For the wider sample of literature eclipse

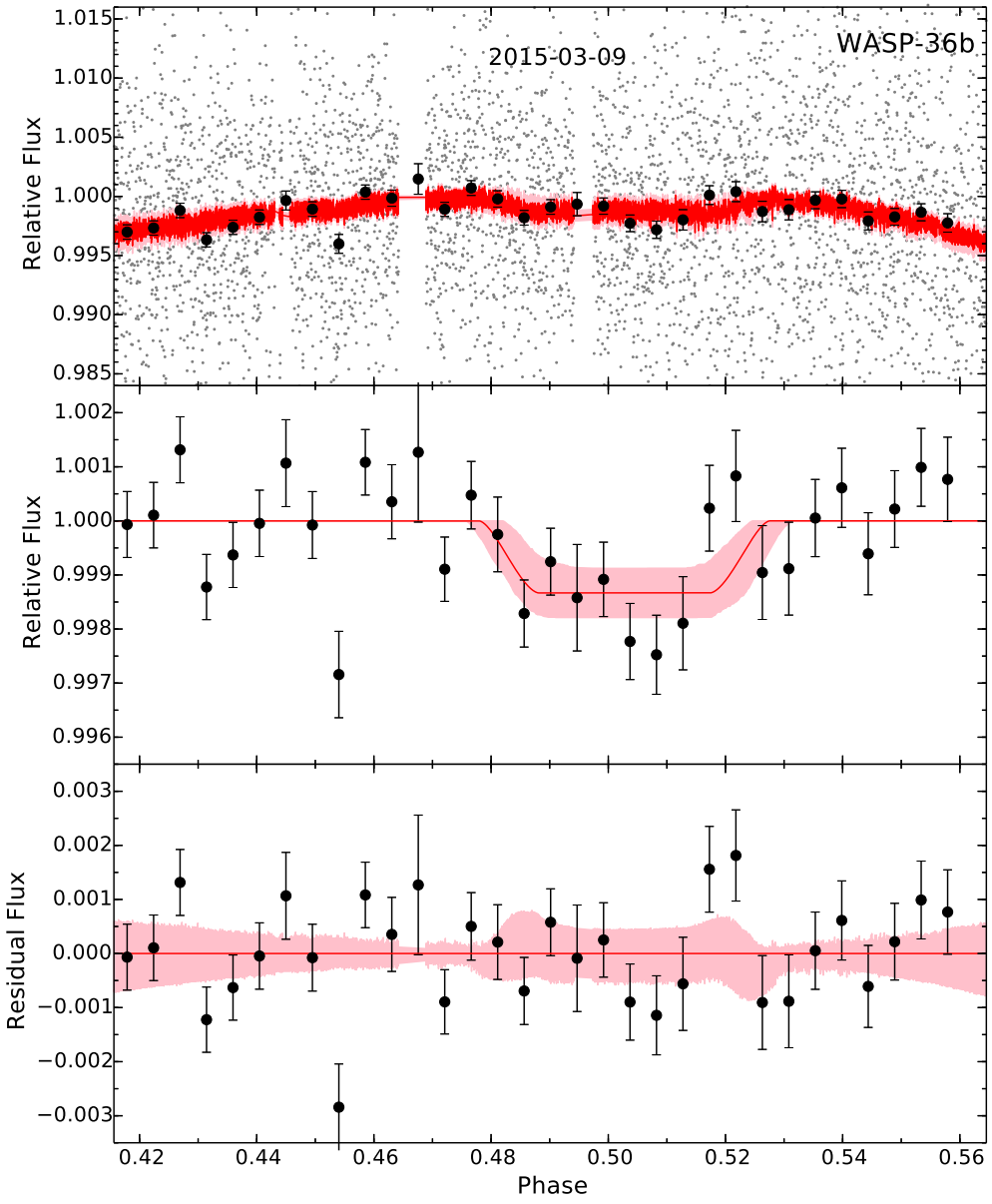

Figure 5. Light curve for the eclipse event of WASP-36b, plotted as per the description for Fig. 1.

measurements, the uncertainties in the eclipse depths are also often underestimated; the scatter in repeated eclipse depths reported for the same planet is 1.4 times larger than the mean error estimates for *Ks*-band observations (Zhou et al. 2014), and two times larger for *Spitzer* measurements (Hansen, Schwartz & Cowan 2014).

However, eclipse measurements remain intrinsically difficult due to the low signal-to-noise nature of the planetary eclipse and the variety of systematic signals that can be introduced. Time-correlated noise often still remains in our observations despite decorrelation against the instrumental model, as most of the light-curve residuals have $\beta > 1$. In cases where the time-correlated noise is significant (e.g. observations of WASP-36b and WASP-76b), we notice the uncertainties in the eclipse depth are larger than other eclipses of equivalent depths.

With these caveats, we can place our observations in the context of the hot-Jupiter atmospheres sample. In this section, we empirically examine the colour–magnitude distributions and brightness–equilibrium temperature distributions of the hot-Jupiter population.

4.1 Colour–magnitude diagram

We compare the broad-band colours and magnitudes of the planets examined in this study with other hot-Jupiters, brown dwarfs, and late M-dwarfs. Brown dwarfs and late M-dwarfs have similar effective temperatures as the equilibrium temperatures of hot-Jupiters, but higher surface gravities, and experience different levels of irradiation to hot-Jupiters. In addition, brown dwarf atmospheres are relatively better understood, and brown dwarf spectral models are the source from which most hot-Jupiter atmosphere models are built. Colour–magnitude and colour–colour diagrams can help compare the broad-band spectra hot-Jupiters, and examine for differences between the atmospheres of hot-Jupiters and brown dwarfs (e.g. Marois et al. 2008; Triaud 2014; Triaud et al. 2014).

To calculate the absolute magnitudes of the hot-Jupiters, we first derive absolute magnitudes for their host stars. The published effective temperature, surface gravity, and metallicity of the host stars are fitted to the Dartmouth isochrones (Dotter et al. 2008), from

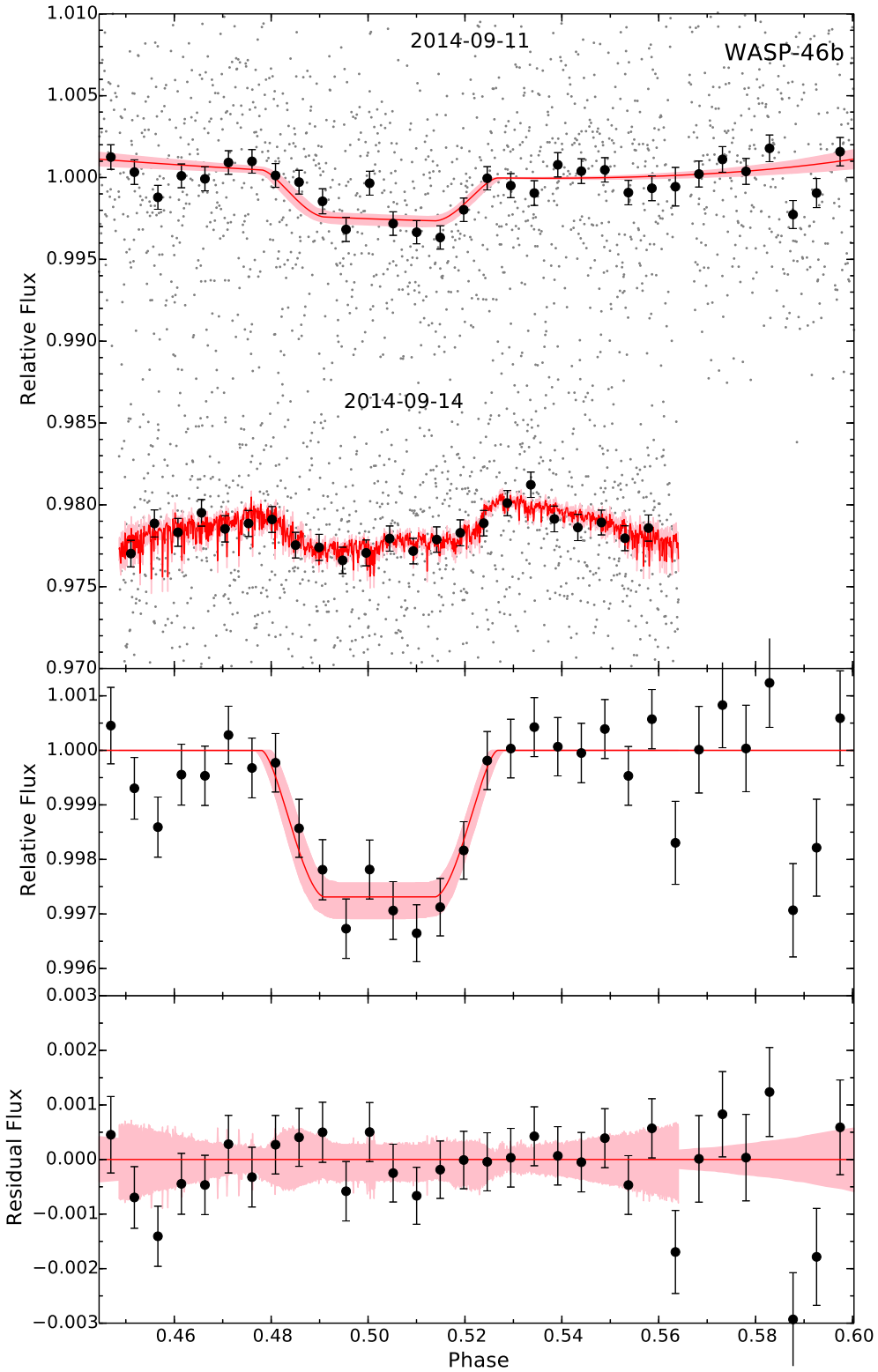

Figure 6. Light curves for the eclipse events of WASP-46b, as measured from 2014-09-11 and 2014-09-14, plotted as per the description for Fig. 2.

which the absolute magnitudes at *K*s and the *Spitzer* IRAC bands are extracted. To propagate the uncertainties, we draw 10^3 iterations of the stellar atmospheric parameters from Gaussian distributions about their reported mean and uncertainty values. For the seven host stars that have *Hipparcos* distances (identified in Triaud 2014), the isochrone derived *J*, *H*, *K* distance modulus agree with that measured from parallax, with 0.2 mag scatter in the residuals. We set 0.2 mag as the lower limit for the absolute magnitude uncertainties we calculate from isochrones. We then calculate the absolute magnitudes of the planets using the measured eclipse depth values and uncertainties. In the cases where repeated observations are available, we calculate a weighted mean eclipse depth and a weighted

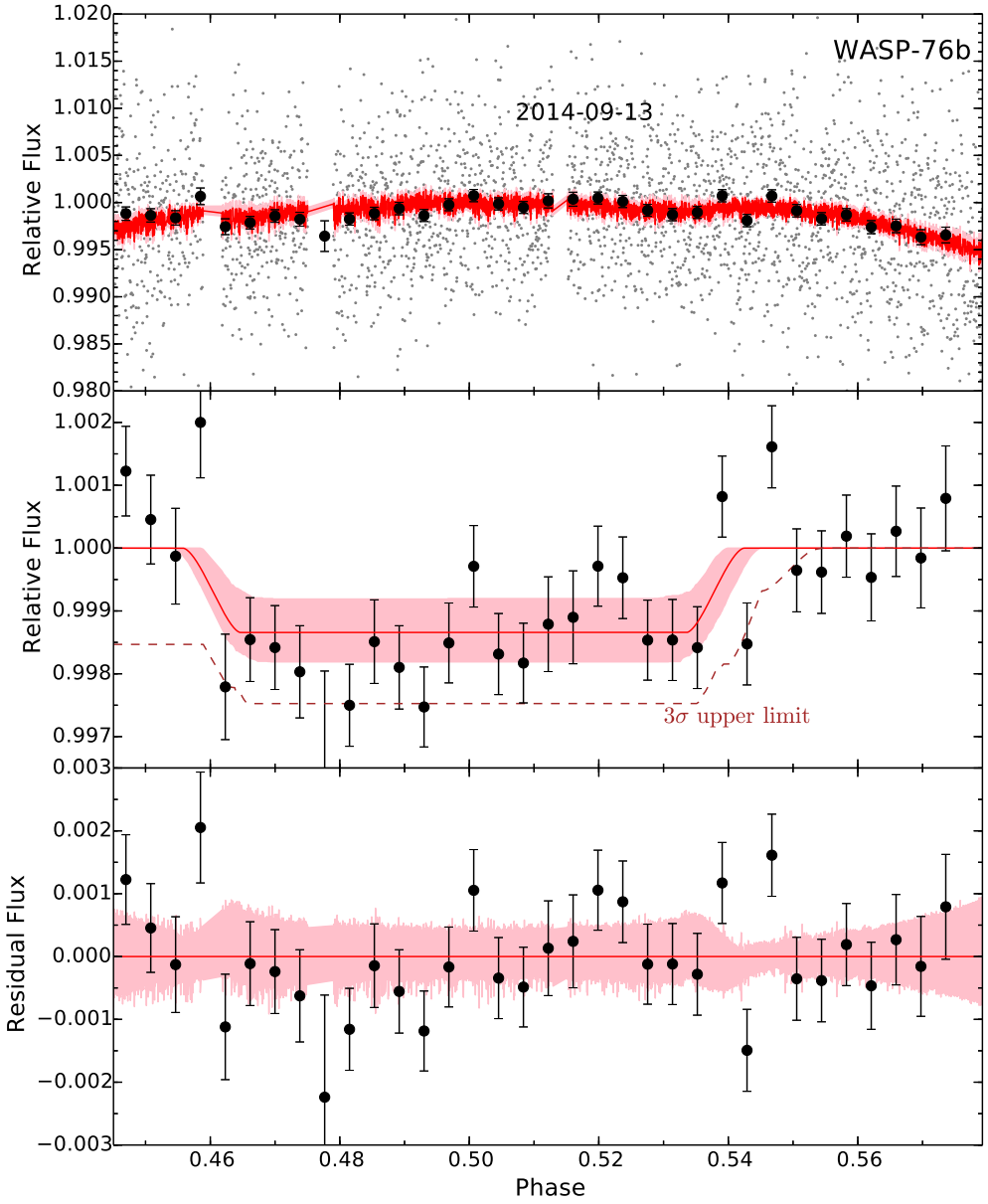

Figure 7. Light curve for the eclipse event of WASP-76b, plotted as per the description for Fig. 1.

standard error in the mean for the uncertainty. The literature eclipse measurements are listed in Appendix A, and gathered partially from the Exoplanet Orbit Database[1] (Han et al. 2014) and table 3 from Bailey (2014). Hot-Jupiters in high-eccentricity orbits (HD 80606b, WASP-8b) were excluded from the list as they are not representative of the hot-Jupiter sample.

Fig. 9 plots the $Ks - [3.6]$ and $Ks - [4.5]$ colours of the hot-Jupiters and brown dwarfs against the $M_{[3.6]}$ and $M_{[4.5]}$ band absolute magnitudes. These bands are chosen as they have the most number of eclipse measurements. The hot-Jupiters are plotted in colour to represent their equilibrium temperatures, with point sizes indicating their planet radii. Brown dwarfs compiled from Dupuy & Liu (2012) are plotted in grey-scale to represent their spectral classes. Model colours from BT-Settl (Allard, Homeier & Freytag 2012), with abundances from Asplund et al. (2009), are plotted for reference.

The sampled hot-Jupiters reside around the M–L spectral classes. The colours of hot-Jupiters are consistent with the colours of brown dwarfs. The $Ks - [4.5]$ colours are marginally redder for the hot-Jupiters than brown dwarfs. A discrepancy between the two populations based on 4.5 μm-related colours was suggested by Triaud et al. (2014), with the mechanism being the absence of absorbing spectral features at 4.5 μm for hot-Jupiters compared to brown dwarfs. The transiting irradiated brown dwarf KELT-1b (Siverd et al. 2012) is also plotted. It is the only brown dwarf, receiving similar irradiation levels as hot-Jupiters, with secondary eclipse measurements. The colours of KELT-1b matches well with that of isolated brown dwarfs and brown dwarf atmosphere models.

For a direct comparison of the spectral properties of hot-Jupiters and brown dwarfs, we plot their $Ks - [3.6]$ versus $Ks - [4.5]$ colour–colour relationship in Fig. 10. This removes the luminosity

[1] This research has made use of the Exoplanet Orbit Database and the Exoplanet Data Explorer at exoplanets.org.

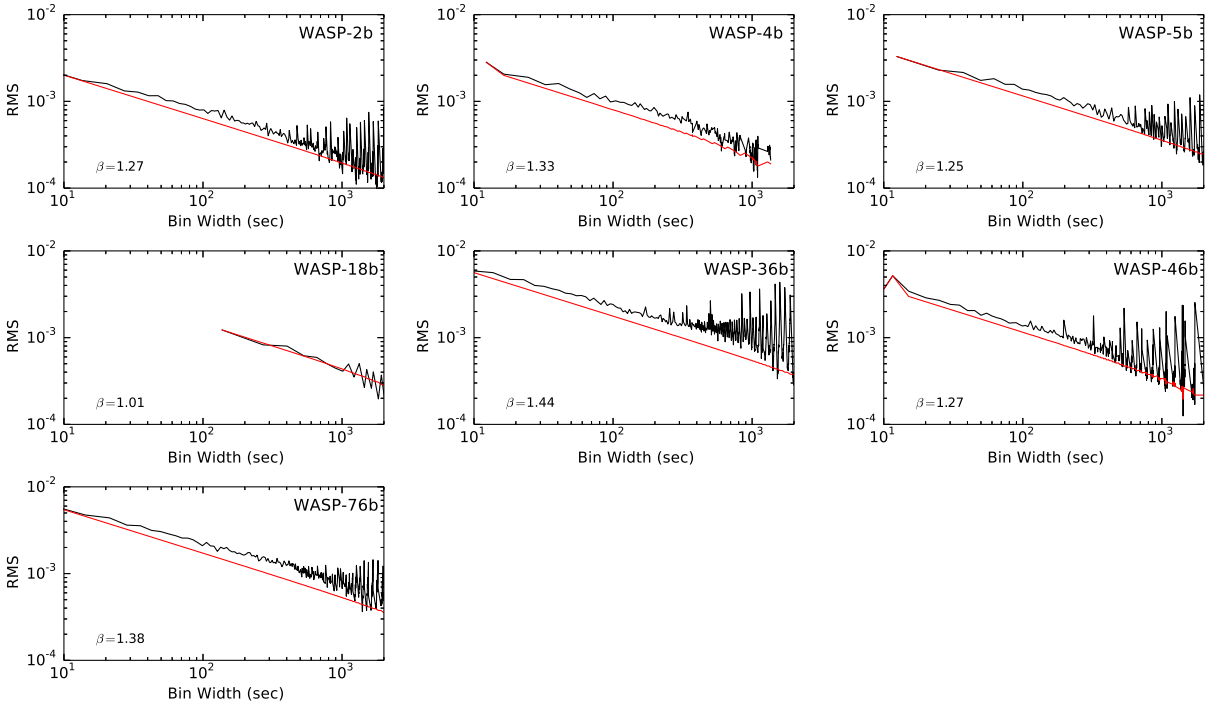

Figure 8. The rms of the light curve residuals, with the eclipse and external parameter models subtracted, as a function of the bin sizes. The red line plots the expected rms assuming no time-correlated noise, where the binned scatter scales $1/\sqrt{n}$. We calculate the average β factor for each set of observations, which measures level of time correlation within the data binned at time-scales between 60 and 600 s. $\beta > 1$ indicates the presence of time-correlated noise in the residuals, while $\beta = 1$ indicates residuals scale with the bin size.

dependence on radius and reduces the scatter in the distribution. Here, it is interesting to note that the current sample of hot-Jupiter colours matches well with that of brown dwarfs.

We expect a greater diversity in the hot-Jupiter spectral properties compared to brown dwarfs. Hot-Jupiters have radii that differ by a factor of 2 between similar mass planets, and have atmospheres that are heated from above and below at different levels of irradiation, resulting in a wide range of possible pressure–temperature profiles. We therefore expect the colour distribution of hot-Jupiters to exhibit significantly greater scatter than that of brown dwarfs. However, the scatter in the colour distribution is currently dominated by the measurement uncertainties of the eclipse observations. Further repeated observations, for robust colour measurements, and a greater sample size, may help distinguish between the brown dwarf and planet population.

4.2 Brightness–equilibrium temperature distribution

3D models investigating the circulation of strongly irradiated hot-Jupiters have predicted large day-night temperature differences, with the most irradiated planets developing strong, superrotating, equatorial jets, and large longitudinal temperature gradients (e.g. Showman & Guillot 2002; Dobbs-Dixon & Lin 2008). These have been revealed by observations of infrared phase curves with peaks offset from the sub-stellar point (e.g. Knutson et al. 2007; Stevenson et al. 2014a; Zellem et al. 2014). Showman, Lewis & Fortney (2015) have shown the extent of this day–night temperature difference is dependent on the level of irradiation and the rotation rate of the planet. In comparison, the circulation of mildly irradiated and/or rapidly rotating hot-Jupiters are expected to be dominated by latitudinal variation, and weaker longitudinal differences.

To probe for a boundary between the mildly irradiated, thermally well-mixed hot-Jupiters, and the strongly-irradiated hot-Jupiters, Cowan & Agol (2011) and Schwartz & Cowan (2015) used the available multiband eclipse observations to compare dayside effective temperatures of hot-Jupiters with their expected equilibrium temperatures. They tentatively identified two populations of hot-Jupiters, with the most irradiated planets having lower heat recirculation efficiencies, and higher relative effective temperature, than mildly irradiated hot-Jupiters.

We re-examine this proposed dichotomy for the photometric bands where a significant number of hot-Jupiters have been sampled in eclipse. Each infrared band probes a different layer of the planetary atmosphere, with shorter wavelengths probing higher pressure regions, where models predict better thermal mixing than at higher altitudes. For each planet sampled in each of the *K*s and *Spitzer* IRAC bands, we calculate an equilibrium temperature $T_{\rm eq}$, assuming zero albedo and no heat redistribution. The uncertainty on the equilibrium temperature is calculated from 10^3 iterations of random sampling, such that errors in the semimajor axis, stellar radius, and stellar effective temperature are propagated. For each band, we calculate a brightness temperature $T_{\rm B}$ from the reported average eclipse depths (listed in appendix A). The $T_{\rm eq}$ of each planet and each band is plotted against the normalized $T_{\rm B}/T_{\rm eq}$ ratio in Fig. 11.

To test for multiple populations within the $T_{\rm B}/T_{\rm eq}$ distribution, we apply the moving two-sample Kolmogorov–Smirnov (K–S) test and the Gaussian mixture model (GMM) analyses. These techniques have previously been used to check for distinct populations in the metallicity–planet radius (Buchhave et al. 2014; Schlaufman 2015) and metallicity–planet period distributions (Zhu 2015).

In a moving K–S test, we split the population into two samples along a series of $T_{\rm eq}$ values, and in each instance calculate the K–S

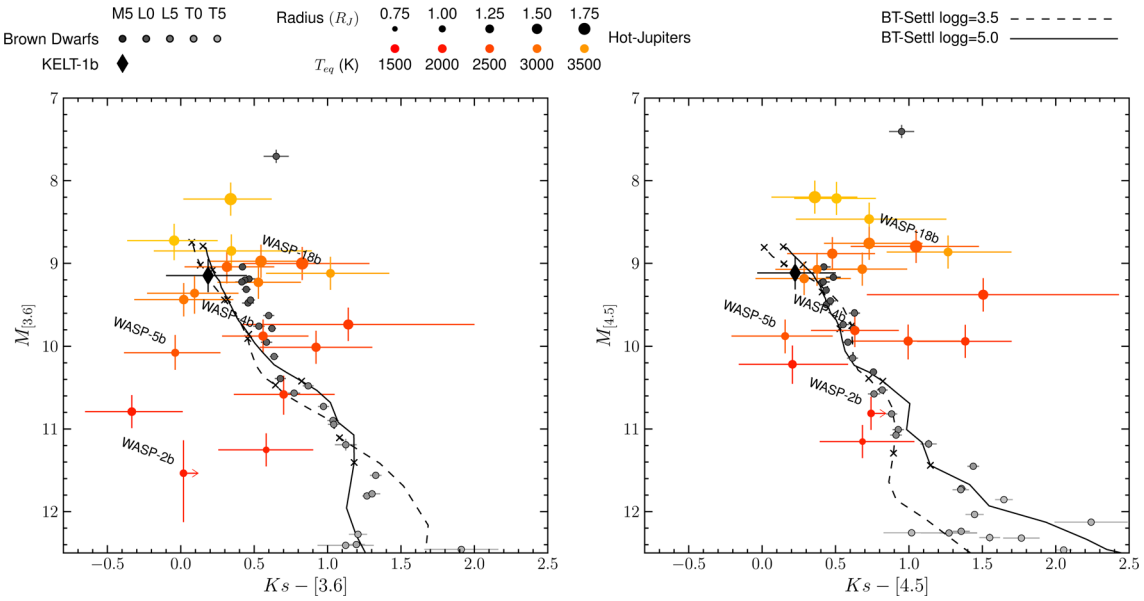

Figure 9. Colour–magnitude diagrams for hot-Jupiters and brown dwarfs. Hot-Jupiters are plotted in colour according to their equilibrium temperature, and with point sizes relative to their planet radii. The planets with *Ks*-band eclipses reported in this paper, and with available *Spitzer* eclipse observations, are labelled. Where appropriate, upper limits in the colour axis are given. The transiting brown dwarf KELT-1b is plotted as the black diamond. It is the only irradiated brown dwarf with secondary eclipse measurements available. The colour–magnitudes of brown dwarfs with parallaxes and photometry compiled by Dupuy & Liu (2012) are plotted for comparison, the points are grey-scaled according to spectral class. The BT-Settl model colours, from <4000 K, are marked by the black lines. The corresponding effective temperatures of the models are marked by crosses every 500 K. Models at $\log g = 3.5$ and 5.0, corresponding to the surface gravities of Jupiter and typical brown dwarfs, are marked by the dashed and solid lines, respectively. The absolute magnitudes for the models are converted assuming 1 R_J objects. References for the parallaxes of the points plotted are Andrei et al. (2011), Artigau et al. (2010), Benedict et al. (1999), Costa et al. (2005), Costa et al. (2006), Dahn et al. (2002), Dupuy & Liu (2012), Gatewood & Coban (2009), Geyer, Harrington & Worley (1988), Harrington et al. (1993), Henry et al. (2006), Kirkpatrick et al. (2011), Lépine et al. (2009), Marocco et al. (2010), Monet et al. (1992), Reid et al. (2003), Schilbach, Röser & Scholz (2009), Subasavage et al. (2009), Teixeira et al. (2008), Tinney et al. (1995), Tinney (1996), Tinney, Burgasser & Kirkpatrick (2003), van Altena, Lee & Hoffleit (1995), van Leeuwen (2007), Vrba et al. (2004). References for the 2MASS photometry used are Biller et al. (2010), Bonnefoy et al. (2011), Chiu et al. (2006), Close et al. (2002), Currie et al. (2011), Cutri et al. (2003), Deacon et al. (2012), Dupuy, Liu & Bowler (2009b), Dupuy, Liu & Ireland (2009b), Dupuy et al. (2010), Dupuy & Liu (2012), Esposito et al. (2013), Forrest, Shure & Skrutskie (1988), Galicher et al. (2011), Golimowski et al. (2004), Henry & McCarthy (1993), Hewett et al. (2006), Janson et al. (2011), Jones et al. (1996), Kasper et al. (2007), King et al. (2010), Kirkpatrick et al. (2011), Knapp et al. (2004), Konopacky et al. (2010), Lane et al. (2001), Leggett, Allard & Hauschildt (1998), Leggett et al. (2000), Leggett et al. (2001), Leggett et al. (2002b), Leggett et al. (2002a), Leggett et al. (2007), Liu et al. (2006), Liu, Dupuy & Ireland (2008), Liu, Dupuy & Leggett (2010), Lodieu et al. (2007), Lowrance et al. (2000), Marois et al. (2008), Marois et al. (2010), Metchev & Hillenbrand (2006), Mugrauer, Seifahrt & Neuhäuser (2007), Nielsen et al. (2012), Reid & Cruz (2002). References for the IRAC photometry used are Kirkpatrick et al. (2011), Leggett et al. (2007), Liu et al. (2010), Luhman et al. (2012), Patten et al. (2006), Wright et al. (2010).

test *p*-values to test the null hypothesis that the T_B/T_{eq} distribution for the two samples originate from the same population. If a significant minimum is observed in the T_{eq}–*p*-value relationship, then we can state that the distribution is made of two distinct populations. To propagate the uncertainties in T_{eq} and T_B, we perform the moving K–S test 10^3 times, at each iteration drawing each point from distributions about its mean and error. The T_{eq}–*p*-value relationship from the moving K–S test is plotted in Fig. 12. We recover the weak division suggested by Cowan & Agol (2011) in all the *Spitzer* bands, finding a tentative division at 2170, 2590, 2440, and 2380 K in the 3.6, 4.5, 5.8, and 8.0 μm bands. There appears to be no significant division in the *Ks* band, with the lack of a clear minimum in the T_{eq}–*p*-value relationship. However, the division is statistically insignificant in all of the bands, with the minimum *p*-value consistently ≥0.05.

Schlaufman (2015) suggested modelling the populations as Gaussian mixtures as a more rigorous way of distinguishing between multiple clusters in the population. We employ the GMM clustering function in the PYTHON package SCIKIT-LEARN (Pedregosa et al. 2012). We fit the T_{eq}–T_B/T_{eq} distribution with GMMs consisting of $N = 1, 2, \ldots, 5$ full Gaussian components. The model that minimizes the BIC is chosen as the best-fitting model. To take into account the per point uncertainties, we draw the population from their measurement uncertainties 10^3 times, each time performing the BIC calculation and model selection. We find that the single component model is preferred for the T_{eq}–T_B/T_{eq} distribution at every band. The $N \geq 2$ component models are rejected >90 per cent of the time in the *Ks*, 4.5, 5.8, and 8.0 μm bands, and >60 per cent of the time for the 3.6 μm band. We find a lack of conclusive evidence that the eclipse sample can be split into two populations.

Given the limits of the current data, these tests show that the atmospheric circulation properties of the hot-Jupiter population is continuous. We suggest that there is likely no sharp divide between the warm Jupiters dominated by latitudinal circulation and the hot-Jupiters with longitudinal circulation.

However, if we were to force a two-component fit to the GMM, we find a relatively consistent result between the groups identified in each band. There is also a consistency in the 4.5, 5.8, and 8.0 μm bands between the divisions identified by the moving K–S test and the division between clusters found by GMM. Fig. 11 colour codes each planet according to the classifications from the two-component GMM fit.

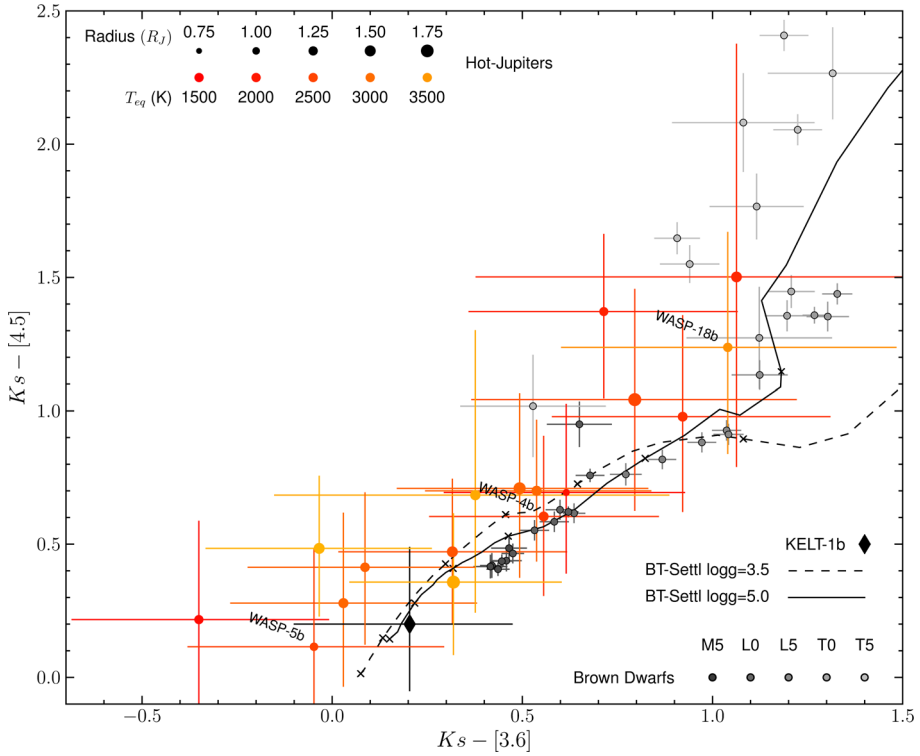

Figure 10. $Ks - [3.6]$ versus $Ks - [4.5]$ colour–colour diagram for hot-Jupiters and brown dwarfs. Colour–colour diagrams reduce the effect of the large scatter in planet radii, therefore luminosity, on the spectral-class comparisons. The plot markings and references are the same as Fig. 9.

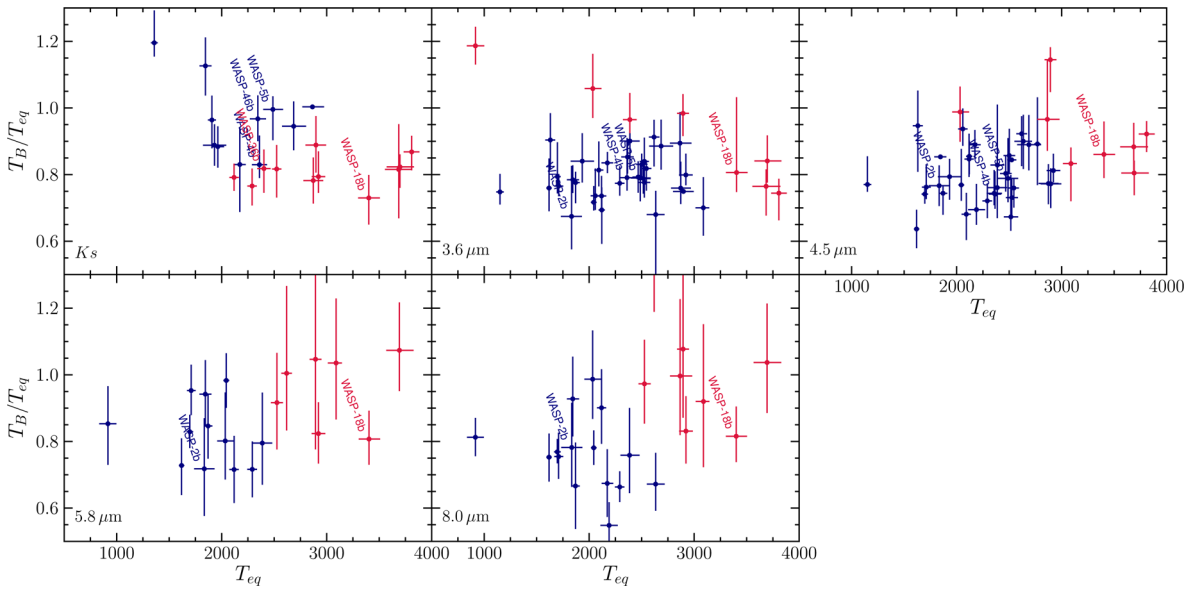

Figure 11. The normalized brightness temperature T_B/T_{eq} – equilibrium temperature T_{eq} distribution from secondary eclipses measured at near-infrared bands. The hot-Jupiters with *Ks* band eclipses reported in this paper, and with relevant *Spitzer*-band observations, are labelled. Gaussian mixture model (GMM) clustering preferentially selects a single component model for the distribution at all the bands. The blue and red colours show the clusters if we force a $N = 2$ component fit to the distributions.

The difference between the mean T_B/T_{eq} between the two clusters is increasing with wavelength. The difference in the mean is 0.03 ± 0.18 at the *Ks* band, and 0.24 ± 0.20 at [8.0]. Longer wavelength probe the upper planetary atmosphere, where the day–night temperature gradient is expected to be highest, whilst better thermal mixing is expected at higher pressures deeper in the atmosphere. The same effect should also lead to a larger difference between the two proposed hot-Jupiter populations at longer wavelengths, as demonstrated by this trend. We suspect that an underlying smooth transition may exist, but must await a larger sample size before becoming statistically significant.

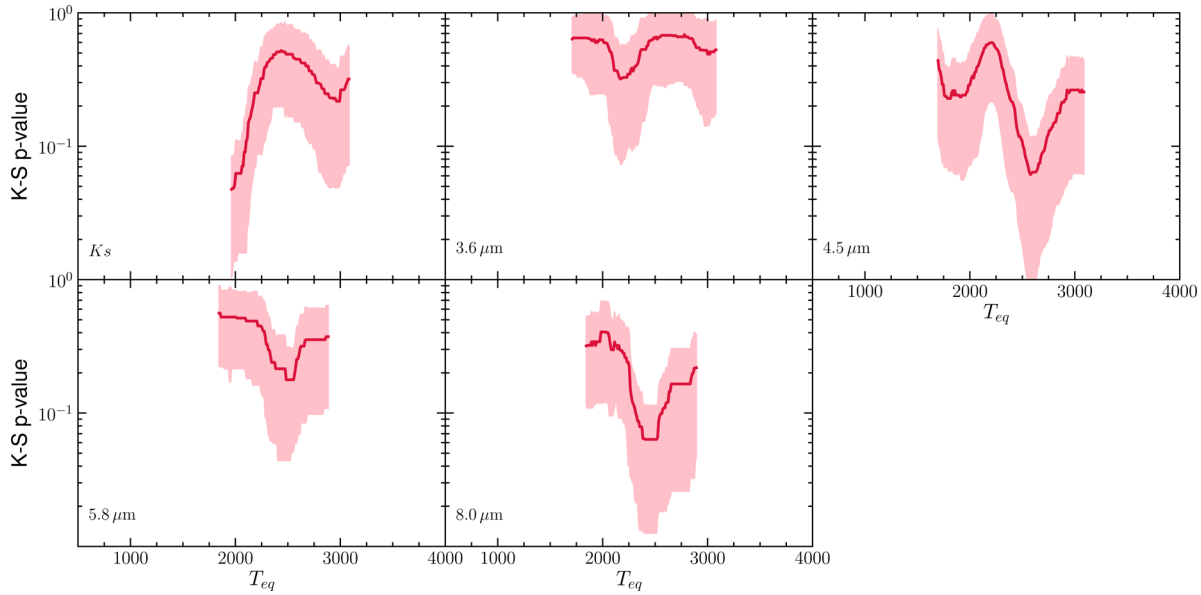

Figure 12. The p-value–T_{eq} relation from a moving K–S test along the T_B/T_{eq}–T_{eq} distribution. Minima in the p-values should indicate divisions between distinct populations in the sample. We find no significant p-value minima (all >0.05), indicating a lack of significant division in the population at all the bands.

ACKNOWLEDGEMENTS

This work is based on observations obtained at the Anglo-Australian Telescope, Siding Spring, Australia. We thank the support of the AAO staff who helped with establishing the observing strategy employed in this work. CGT gratefully acknowledges the support of ARC Australian Professorial Fellowship grant DP0774000 and ARC Discovery Outstanding Researcher Award DP130102695.

REFERENCES

Allard F., Homeier D., Freytag B., 2012, Phil. Trans. R. Soc. A, 370, 2765
Alonso R., Deeg H. J., Kabath P., Rabus M., 2010, AJ, 139, 1481
Anderson D. R. et al., 2008, MNRAS, 387, L4
Anderson D. R. et al., 2011, MNRAS, 416, 2108
Anderson D. R. et al., 2012, MNRAS, 422, 1988
Anderson D. R. et al., 2013, MNRAS, 430, 3422
Andrei A. H. et al., 2011, AJ, 141, 54
Artigau É., Radigan J., Folkes S., Jayawardhana R., Kurtev R., Lafrenière D., Doyon R., Borissova J., 2010, ApJ, 718, L38
Asplund M., Grevesse N., Sauval A. J., Scott P., 2009, ARA&A, 47, 481
Bailey J., 2014, PASA, 31, 43
Baskin N. J. et al., 2013, ApJ, 773, 124
Beatty T. G. et al., 2014, ApJ, 783, 112
Beerer I. M. et al., 2011, ApJ, 727, 23
Benedict G. F. et al., 1999, AJ, 118, 1086
Bertin E., Arnouts S., 1996, A&AS, 117, 393
Biller B. A. et al., 2010, ApJ, 720, L82
Blecic J. et al., 2013, ApJ, 779, 5
Blecic J. et al., 2014, ApJ, 781, 116
Bonnefoy M. et al., 2011, A&A, 528, L15
Buchhave L. A. et al., 2014, Nature, 509, 593
Cáceres C. et al., 2011, A&A, 530, A5
Charbonneau D. et al., 2005, ApJ, 626, 523
Charbonneau D., Knutson H. A., Barman T., Allen L. E., Mayor M., Megeath S. T., Queloz D., Udry S., 2008, ApJ, 686, 1341
Chen G. et al., 2014a, A&A, 563, A40
Chen G., van Boekel R., Madhusudhan N., Wang H., Nikolov N., Seemann U., Henning T., 2014b, A&A, 564, A6
Chen G., van Boekel R., Wang H., Nikolov N., Seemann U., Henning T., 2014c, A&A, 567, A8
Chiu K., Fan X., Leggett S. K., Golimowski D. A., Zheng W., Geballe T. R., Schneider D. P., Brinkmann J., 2006, AJ, 131, 2722
Christiansen J. L. et al., 2010, ApJ, 710, 97
Close L. M., Siegler N., Potter D., Brandner W., Liebert J., 2002, ApJ, 567, L53
Collier Cameron A. et al., 2007, MNRAS, 375, 951
Costa E., Méndez R. A., Jao W.-C., Henry T. J., Subasavage J. P., Brown M. A., Ianna P. A., Bartlett J., 2005, AJ, 130, 337
Costa E., Méndez R. A., Jao W.-C., Henry T. J., Subasavage J. P., Ianna P. A., 2006, AJ, 132, 1234
Cowan N. B., Agol E., 2011, ApJ, 729, 54
Croll B., Albert L., Lafreniere D., Jayawardhana R., Fortney J. J., 2010a, ApJ, 717, 1084
Croll B., Jayawardhana R., Fortney J. J., Lafrenière D., Albert L., 2010b, ApJ, 718, 920
Croll B., Lafreniere D., Albert L., Jayawardhana R., Fortney J. J., Murray N., 2011, AJ, 141, 30
Croll B. et al., 2015, ApJ, 802, 28
Cruz P., Barrado D., Lillo-Box J., Diaz M., Birkby J., López-Morales M., Hodgkin S., Fortney J. J., 2015, A&A, 574, A103
Cubillos P., Harrington J., Madhusudhan N., Foster A. S. D., Lust N. B., Hardy R. A., Bowman M. O., 2014, ApJ, 797, 42
Currie T., Thalmann C., Matsumura S., Madhusudhan N., Burrows A., Kuchner M., 2011, ApJ, 736, L33
Cutri R. M. et al., 2003, 2MASS All Sky Catalog of Point Sources. NASA/IPAC Infrared Science Archive. Available at: http://irsa.ipac.caltech.edu/applications/Gator/
Dahn C. C. et al., 2002, AJ, 124, 1170
de Mooij E. J. W., Snellen I. A. G., 2009, A&A, 493, L35
de Mooij E. J. W., de Kok R. J., Nefs S. V., Snellen I. A. G., 2011, A&A, 528, A49
de Mooij E. J. W., Brogi M., de Kok R. J., Snellen I. A. G., Kenworthy M. A., Karjalainen R., 2013, A&A, 550, A54
Deacon N. R. et al., 2012, ApJ, 755, 94
Deming D., Harrington J., Laughlin G., Seager S., Navarro S. B., Bowman W. C., Horning K., 2007, ApJ, 667, L199
Deming D. et al., 2011, ApJ, 726, 95
Deming D. et al., 2012, ApJ, 754, 106
Deming D. et al., 2015, ApJ, 805, 132
Demory B.-O. et al., 2007, A&A, 475, 1125
Demory B.-O., Gillon M., Seager S., Benneke B., Deming D., Jackson B., 2012, ApJ, 751, L28

Désert J.-M. et al., 2011a, ApJS, 197, 11
Désert J.-M. et al., 2011b, ApJS, 197, 14
Dobbs-Dixon I., Lin D. N. C., 2008, ApJ, 673, 513
Dobbs-Dixon I., Lin D. N. C., Mardling R. A., 2004, ApJ, 610, 464
Dotter A., Chaboyer B., Jevremović D., Kostov V., Baron E., Ferguson J. W., 2008, ApJS, 178, 89
Dupuy T. J., Liu M. C., 2012, ApJS, 201, 19
Dupuy T. J., Liu M. C., Ireland M. J., 2009a, ApJ, 699, 168
Dupuy T. J., Liu M. C., Bowler B. P., 2009b, ApJ, 706, 328
Dupuy T. J., Liu M. C., Bowler B. P., Cushing M. C., Helling C., Witte S., Hauschildt P., 2010, ApJ, 721, 1725
Eastman J., Siverd R., Gaudi B. S., 2010, PASP, 122, 935
Esposito S. et al., 2013, A&A, 549, A52
Foreman-Mackey D., Hogg D. W., Lang D., Goodman J., 2013, PASP, 125, 306
Forrest W. J., Shure M., Skrutskie M. F., 1988, ApJ, 330, L119
Fortney J. J. et al., 2011, ApJS, 197, 9
Fressin F., Knutson H. A., Charbonneau D., O'Donovan F. T., Burrows A., Deming D., Mandushev G., Spiegel D., 2010, ApJ, 711, 374
Galicher R., Marois C., Macintosh B., Barman T., Konopacky Q., 2011, ApJ, 739, L41
Gatewood G., Coban L., 2009, AJ, 137, 402
Geyer D. W., Harrington R. S., Worley C. E., 1988, AJ, 95, 1841
Gibson N. P. et al., 2010, MNRAS, 404, L114
Gillon M. et al., 2009, A&A, 506, 359
Gillon M. et al., 2010, A&A, 511, A3
Golimowski D. A. et al., 2004, AJ, 127, 3516
Han E., Wang S. X., Wright J. T., Feng Y. K., Zhao M., Fakhouri O., Brown J. I., Hancock C., 2014, PASP, 126, 827
Hansen C. J., Schwartz J. C., Cowan N. B., 2014, MNRAS, 444, 3632
Harrington R. S. et al., 1993, AJ, 105, 1571
Hartman J. D. et al., 2008, ApJ, 675, 1233
Hellier C. et al., 2009, Nature, 460, 1098
,Henry T. J., McCarthy, D. W., Jr, 1993, AJ, 106, 773
Henry T. J., Jao W.-C., Subasavage J. P., Beaulieu T. D., Ianna P. A., Costa E., Méndez R. A., 2006, AJ, 132, 2360
Hewett P. C., Warren S. J., Leggett S. K., Hodgkin S. T., 2006, MNRAS, 367, 454
Hoyer S. et al., 2013, MNRAS, 434, 46
Janson M. et al., 2011, ApJ, 728, 85
Jones H. R. A., Longmore A. J., Allard F., Hauschildt P. H., 1996, MNRAS, 280, 77
Kasper M., Biller B. A., Burrows A., Brandner W., Budaj J., Close L. M., 2007, A&A, 471, 655
King R. R., McCaughrean M. J., Homeier D., Allard F., Scholz R.-D., Lodieu N., 2010, A&A, 510, A99
Kirkpatrick J. D. et al., 2011, ApJS, 197, 19
Knapp G. R. et al., 2004, AJ, 127, 3553
Knutson H. A. et al., 2007, Nature, 447, 183
Knutson H. A., Charbonneau D., Allen L. E., Burrows A., Megeath S. T., 2008, ApJ, 673, 526
Knutson H. A., Charbonneau D., Burrows A., O'Donovan F. T., Mandushev G., 2009a, ApJ, 691, 866
Knutson H. A., Charbonneau D., Cowan N. B., Fortney J. J., Showman A. P., Agol E., Henry G. W., 2009b, ApJ, 703, 769
Knutson H. A., Howard A. W., Isaacson H., 2010, ApJ, 720, 1569
Knutson H. A. et al., 2011, ApJ, 735, 27
Knutson H. A. et al., 2012, ApJ, 754, 22
Konopacky Q. M., Ghez A. M., Barman T. S., Rice E. L., Bailey J. I., III, White R. J., McLean I. S., Duchêne G., 2010, ApJ, 711, 1087
Lane B. F., Zapatero Osorio M. R., Britton M. C., Martín E. L., Kulkarni S. R., 2001, ApJ, 560, 390
Lanotte A. A. et al., 2014, A&A, 572, A73
Leggett S. K., Allard F., Hauschildt P. H., 1998, ApJ, 509, 836
Leggett S. K. et al., 2000, ApJ, 536, L35
Leggett S. K., Allard F., Geballe T. R., Hauschildt P. H., Schweitzer A., 2001, ApJ, 548, 908
Leggett S. K., Hauschildt P. H., Allard F., Geballe T. R., Baron E., 2002a, MNRAS, 332, 78
Leggett S. K. et al., 2002b, ApJ, 564, 452
Leggett S. K., Saumon D., Marley M. S., Geballe T. R., Golimowski D. A., Stephens D., Fan X., 2007, ApJ, 655, 1079
Lépine S., Thorstensen J. R., Shara M. M., Rich R. M., 2009, AJ, 137, 4109
Lewis N. K. et al., 2013, ApJ, 766, 95
Liu M. C., Leggett S. K., Golimowski D. A., Chiu K., Fan X., Geballe T. R., Schneider D. P., Brinkmann J., 2006, ApJ, 647, 1393
Liu M. C., Dupuy T. J., Ireland M. J., 2008, ApJ, 689, 436
Liu M. C., Dupuy T. J., Leggett S. K., 2010, ApJ, 722, 311
Lodieu N. et al., 2007, MNRAS, 379, 1423
Lowrance P. J. et al., 2000, ApJ, 541, 390
Luhman K. L., Burgasser A. J., Labbé I., Saumon D., Marley M. S., Bochanski J. J., Monson A. J., Persson S. E., 2012, ApJ, 744, 135
Machalek P., McCullough P. R., Burke C. J., Valenti J. A., Burrows A., Hora J. L., 2008, ApJ, 684, 1427
Machalek P., McCullough P. R., Burrows A., Burke C. J., Hora J. L., Johns-Krull C. M., 2009, ApJ, 701, 514
Machalek P., Greene T., McCullough P. R., Burrows A., Burke C. J., Hora J. L., Johns-Krull C. M., Deming D. L., 2010, ApJ, 711, 111
Marocco F. et al., 2010, A&A, 524, A38
Marois C., Macintosh B., Barman T., Zuckerman B., Song I., Patience J., Lafrenière D., Doyon R., 2008, Science, 322, 1348
Marois C., Zuckerman B., Konopacky Q. M., Macintosh B., Barman T., 2010, Nature, 468, 1080
Maxted P. F. L. et al., 2013, MNRAS, 428, 2645
Metchev S. A., Hillenbrand L. A., 2006, ApJ, 651, 1166
Monet D. G., Dahn C. C., Vrba F. J., Harris H. C., Pier J. R., Luginbuhl C. B., Ables H. D., 1992, AJ, 103, 638
Mugrauer M., Seifahrt A., Neuhäuser R., 2007, MNRAS, 378, 1328
Nelson B., Davis W. D., 1972, ApJ, 174, 617
Nielsen E. L. et al., 2012, ApJ, 750, 53
Nymeyer S. et al., 2011, ApJ, 742, 35
O'Donovan F. T., Charbonneau D., Harrington J., Madhusudhan N., Seager S., Deming D., Knutson H. A., 2010, ApJ, 710, 1551
O'Rourke J. G. et al., 2014, ApJ, 781, 109
Pál A., 2012, MNRAS, 421, 1825
Patten B. M. et al., 2006, ApJ, 651, 502
Pedregosa F. et al., 2012, preprint (arXiv:1201.0490)
Popper D. M., Etzel P. B., 1981, AJ, 86, 102
Reid I. N., Cruz K. L., 2002, AJ, 123, 2806
Reid I. N. et al., 2003, AJ, 125, 354
Rogers J. C., Apai D., López-Morales M., Sing D. K., Burrows A., 2009, ApJ, 707, 1707
Rostron J. W., Wheatley P. J., Anderson D. R., Collier Cameron A., Fortney J. J., Harrington J., Knutson H. A., Pollacco D. L., 2014, MNRAS, 441, 3666
Schilbach E., Röser S., Scholz R.-D., 2009, A&A, 493, L27
Schlaufman K. C., 2015, ApJ, 799, L26
Schwartz J. C., Cowan N. B., 2015, MNRAS, 449, 4192
Showman A. P., Guillot T., 2002, A&A, 385, 166
Showman A. P., Lewis N. K., Fortney J. J., 2015, ApJ, 801, 95
Shporer A. et al., 2014, ApJ, 788, 92
Siverd R. J. et al., 2012, ApJ, 761, 123
Skrutskie M. F. et al., 2006, AJ, 131, 1163
Smith A. M. S. et al., 2012a, AJ, 143, 81
Smith A. M. S. et al., 2012b, A&A, 545, A93
Snellen I. A. G., Covino E., 2007, MNRAS, 375, 307
Southworth J., Maxted P. F. L., Smalley B., 2004, MNRAS, 351, 1277
Southworth J. et al., 2009a, MNRAS, 396, 1023
Southworth J. et al., 2009b, ApJ, 707, 167
Southworth J. et al., 2010, MNRAS, 408, 1680
Stevenson K. B. et al., 2010, Nature, 464, 1161
Stevenson K. B. et al., 2012, ApJ, 754, 136
Stevenson K. B. et al., 2014a, Science, 346, 838
Stevenson K. B., Bean J. L., Madhusudhan N., Harrington J., 2014b, ApJ, 791, 36

Subasavage J. P., Jao W.-C., Henry T. J., Bergeron P., Dufour P., Ianna P. A., Costa E., Méndez R. A., 2009, AJ, 137, 4547
Teixeira R., Ducourant C., Chauvin G., Krone-Martins A., Song I., Zuckerman B., 2008, A&A, 489, 825
Tinney C. G., 1996, MNRAS, 281, 644
Tinney C. G., Reid I. N., Gizis J., Mould J. R., 1995, AJ, 110, 3014
Tinney C. G., Burgasser A. J., Kirkpatrick J. D., 2003, AJ, 126, 975
Tinney C. G. et al., 2004, in Moorwood A. F. M., Iye M., eds, Proc. SPIE Conf. Ser. Vol. 5492, Ground-based Instrumentation for Astronomy. SPIE, Bellingham, p. 998
Todorov K., Deming D., Harrington J., Stevenson K. B., Bowman W. C., Nymeyer S., Fortney J. J., Bakos G. A., 2010, ApJ, 708, 498
Todorov K. O. et al., 2012, ApJ, 746, 111
Todorov K. O. et al., 2013, ApJ, 770, 102
Triaud A. H. M. J., 2014, MNRAS, 439, L61
Triaud A. H. M. J., Lanotte A. A., Smalley B., Gillon M., 2014, MNRAS, 444, 711
Triaud A. H. M. J. et al., 2015, MNRAS, 450, 2279
van Altena W. F., Lee J. T., Hoffleit E. D., 1995, The General Catalogue of Trigonometric [Stellar] Parallaxes. Yale University Observatory, New Haven, CT
van Leeuwen F., ed., 2007, Astrophysics and Space Science Library, Vol. 350, Hipparcos, the New Reduction of the Raw Data. Springer, Berlin
Vrba F. J. et al., 2004, AJ, 127, 2948
Wang W., van Boekel R., Madhusudhan N., Chen G., Zhao G., Henning T., 2013, ApJ, 770, 70
West R. G. et al., 2013, preprint (arXiv:1310.5607)
Wheatley P. J. et al., 2010, preprint (arXiv:1004.0836)
Wilson D. M. et al., 2008, ApJ, 675, L113
Winn J. N. et al., 2008, ApJ, 683, 1076
Wright E. L. et al., 2010, AJ, 140, 1868
Zellem R. T. et al., 2014, ApJ, 790, 53
Zhao M., Monnier J. D., Swain M. R., Barman T., Hinkley S., 2012a, ApJ, 744, 122
Zhao M., Milburn J., Barman T., Hinkley S., Swain M. R., Wright J., Monnier J. D., 2012b, ApJ, 748, L8
Zhao M. et al., 2014, ApJ, 796, 115
Zhou G., Bayliss D. D. R., Kedziora-Chudczer L., Salter G., Tinney C. G., Bailey J., 2014, MNRAS, 445, 2746
Zhu W., 2015, preprint (arXiv:1503.01771)

APPENDIX A: LITERATURE ECLIPSE MEASUREMENTS

Table A1 presents literature eclipse depth measurements for the *K*s, *Spitzer* IRAC 3.6, 4.5, 5.8, 8.0 μm bands.

Table A1. Literature secondary eclipses in the *K*s and *Spitzer* IRAC bands.

Planet	*K*s depth (%)	[3.6] depth (%)	[4.5] depth (%)	[5.8] depth (%)	[8.0] depth (%)	References
55 Cnc e			$0.0131^{+0.0028}_{-0.0028}$			Demory et al. (2012)
CoRoT-1b	$0.278^{+0.043}_{-0.066}$ $0.336^{+0.042}_{-0.042}$	$0.415^{+0.042}_{-0.042}$	$0.482^{+0.042}_{-0.042}$			Gillon et al. (2009); Rogers et al. (2009); Deming et al. (2011)
CoRoT-2b	$0.16^{+0.09}_{-0.09}$	$0.355^{+0.02}_{-0.02}$	$0.51^{+0.042}_{-0.042}$ $0.5^{+0.02}_{-0.02}$		$0.41^{+0.11}_{-0.11}$ $0.446^{+0.1}_{-0.1}$	Alonso et al. (2010); Deming et al. (2011); Gillon et al. (2010)
GJ436b		$0.041^{+0.003}_{-0.003}$	<0.01	$0.033^{+0.014}_{-0.014}$	$0.057^{+0.008}_{-0.008}$ $0.054^{+0.007}_{-0.007}$ $0.054^{+0.008}_{-0.008}$ $0.0452^{+0.0027}_{-0.0027}$	Stevenson et al. (2010); Deming et al. (2007); Demory et al. (2007); Knutson et al. (2011)
HAT-P-1b	$0.109^{+0.025}_{-0.025}$	$0.08^{+0.008}_{-0.008}$	$0.135^{+0.022}_{-0.022}$	$0.203^{+0.031}_{-0.031}$	$0.238^{+0.04}_{-0.04}$	de Mooij et al. (2011); Todorov et al. (2010)
HAT-P-2b		$0.0996^{+0.0072}_{-0.0072}$	$0.1031^{+0.0061}_{-0.0061}$	$0.071^{+0.029}_{-0.013}$	$0.1392^{+0.0095}_{-0.0095}$	Lewis et al. (2013)
HAT-P-3b		$0.112^{+0.015}_{-0.03}$	$0.094^{+0.094}_{-0.009}$			Todorov et al. (2013)
HAT-P-4b		$0.142^{+0.014}_{-0.016}$	$0.122^{+0.012}_{-0.014}$			Todorov et al. (2013)
HAT-P-6b		$0.117^{+0.008}_{-0.008}$	$0.106^{+0.006}_{-0.006}$			Todorov et al. (2012)
HAT-P-7b		$0.098^{+0.017}_{-0.017}$	$0.159^{+0.022}_{-0.022}$	$0.245^{+0.031}_{-0.031}$	$0.225^{+0.052}_{-0.052}$	Christiansen et al. (2010)
HAT-P-8b		$0.131^{+0.007}_{-0.01}$	$0.111^{+0.008}_{-0.007}$			Todorov et al. (2012)
HAT-P-12b		<0.042	<0.085			Todorov et al. (2013)
HAT-P-23b	$0.234^{+0.046}_{-0.046}$	$0.248^{+0.019}_{-0.019}$	$0.309^{+0.026}_{-0.026}$			O'Rourke et al. (2014)
HAT-P-32b	$0.178^{+0.057}_{-0.057}$	$0.364^{+0.016}_{-0.016}$	$0.438^{+0.02}_{-0.02}$			Zhao et al. (2014)
HD149026b		$0.04^{+0.003}_{-0.003}$	$0.034^{+0.006}_{-0.006}$	$0.044^{+0.01}_{-0.01}$	$0.0411^{+0.0076}_{-0.0076}$ $0.052^{+0.006}_{-0.006}$	Stevenson et al. (2012); Knutson et al. (2009b)
HD189733b		$0.256^{+0.014}_{-0.014}$ $0.1466^{+0.004}_{-0.004}$	$0.214^{+0.02}_{-0.02}$ $0.1787^{+0.0038}_{-0.0038}$	$0.31^{+0.034}_{-0.034}$	$0.3381^{+0.0055}_{-0.0055}$ $0.391^{+0.022}_{-0.022}$	Charbonneau et al. (2008); Knutson et al. (2012, 2007)
HD209458b		$0.094^{+0.009}_{-0.009}$	$0.213^{+0.015}_{-0.015}$ $0.1391^{+0.0072}_{-0.0069}$	$0.301^{+0.043}_{-0.043}$	$0.24^{+0.026}_{-0.026}$	Knutson et al. (2008); Zellem et al. (2014)

Table A1 – *continued*

Planet	*Ks* depth (%)	[3.6] depth (%)	[4.5] depth (%)	[5.8] depth (%)	[8.0] depth (%)	References
KELT-1b	$0.160^{+0.018}_{-0.020}$	$0.195^{+0.010}_{-0.010}$	$0.200^{+0.012}_{-0.012}$			Croll et al. (2015); Beatty et al. (2014)
Kepler-5b		$0.103^{+0.017}_{-0.017}$	$0.107^{+0.015}_{-0.015}$			Désert et al. (2011a)
Kepler-6b		$0.069^{+0.027}_{-0.027}$	$0.151^{+0.019}_{-0.019}$			Désert et al. (2011a)
Kepler-12b		$0.137^{+0.02}_{-0.02}$	$0.116^{+0.031}_{-0.031}$			Fortney et al. (2011)
Kepler-13b	$0.122^{+0.051}_{-0.051}$	$0.156^{+0.031}_{-0.031}$	$0.222^{+0.023}_{-0.023}$			Shporer et al. (2014)
Kepler-17b		$0.25^{+0.03}_{-0.03}$	$0.31^{+0.035}_{-0.035}$			Désert et al. (2011b)
OGLE-TR-113b	$0.17^{+0.05}_{-0.05}$					Snellen & Covino (2007)
Qatar-1b	$0.136^{+0.034}_{-0.034}$					Croll et al. (2015)
TrES-1b		$0.083^{+0.024}_{-0.024}$	$0.066^{+0.013}_{-0.013}$ $0.094^{+0.024}_{-0.024}$	$0.152^{+0.042}_{-0.042}$	$0.225^{+0.036}_{-0.036}$ $0.213^{+0.042}_{-0.042}$	Cubillos et al. (2014); Charbonneau et al. (2005)
TrES-2b	$0.062^{+0.013}_{-0.011}$	$0.127^{+0.021}_{-0.021}$	$0.23^{+0.024}_{-0.024}$	$0.199^{+0.054}_{-0.054}$	$0.359^{+0.06}_{-0.06}$	Croll et al. (2010a); O'Donovan et al. (2010)
TrES-3b	$0.241^{+0.043}_{-0.043}$ $0.133^{+0.018}_{-0.016}$	$0.346^{+0.035}_{-0.035}$	$0.372^{+0.054}_{-0.054}$	$0.449^{+0.097}_{-0.097}$	$0.475^{+0.046}_{-0.046}$	de Mooij & Snellen (2009); Croll et al. (2010b); Fressin et al. (2010)
TrES-4b		$0.137^{+0.011}_{-0.011}$	$0.148^{+0.016}_{-0.016}$	$0.261^{+0.059}_{-0.059}$	$0.318^{+0.044}_{-0.044}$	Knutson et al. (2009a)
WASP-1b		$0.184^{+0.016}_{-0.016}$	$0.217^{+0.017}_{-0.017}$	$0.274^{+0.058}_{-0.058}$	$0.474^{+0.046}_{-0.046}$	Wheatley et al. (2010)
WASP-2b	<0.07	$0.083^{+0.035}_{-0.035}$	$0.169^{+0.017}_{-0.017}$	$0.192^{+0.077}_{-0.077}$	$0.285^{+0.059}_{-0.059}$	Wheatley et al. (2010); This Work
WASP-3b	$0.181^{+0.02}_{-0.02}$ $0.193^{+0.014}_{-0.014}$	$0.209^{+0.04}_{-0.028}$	$0.282^{+0.012}_{-0.012}$		$0.328^{+0.086}_{-0.055}$	Zhao et al. (2012b); Croll et al. (2015); Rostron et al. (2014)
WASP-4b	$0.185^{+0.014}_{-0.013}$ $0.16^{+0.04}_{-0.04}$	$0.319^{+0.031}_{-0.031}$	$0.343^{+0.027}_{-0.027}$			Cáceres et al. (2011); Beerer et al. (2011); This Work
WASP-5b	$0.269^{+0.062}_{-0.062}$ $0.20^{+0.02}_{-0.02}$	$0.197^{+0.028}_{-0.028}$	$0.237^{+0.024}_{-0.024}$			Chen et al. (2014b); Baskin et al. (2013); This Work
WASP-10b	$0.137^{+0.013}_{-0.019}$					Cruz et al. (2015)
WASP-12b	$0.299^{+0.065}_{-0.065}$ $0.296^{+0.014}_{-0.014}$	$0.421^{+0.011}_{-0.011}$	$0.428^{+0.012}_{-0.012}$	$0.696^{+0.06}_{-0.06}$	$0.696^{+0.096}_{-0.096}$	Zhao et al. (2012a); Croll et al. (2015); Stevenson et al. (2014b)
WASP-14b		$0.224^{+0.01}_{-0.19}$	$0.224^{+0.018}_{-0.018}$		$0.181^{+0.022}_{-0.022}$	Blecic et al. (2013)
WASP-17b			$0.229^{+0.013}_{-0.013}$		$0.237^{+0.039}_{-0.039}$	Anderson et al. (2011)
WASP-18b	$0.13^{+0.03}_{-0.03}$	$0.3^{+0.02}_{-0.02}$ $0.304^{+0.019}_{-0.019}$	$0.37^{+0.03}_{-0.03}$ $0.379^{+0.015}_{-0.015}$	$0.37^{+0.03}_{-0.03}$	$0.41^{+0.02}_{-0.02}$	Nymeyer et al. (2011); Maxted et al. (2013); This Work
WASP-19b	$0.366^{+0.072}_{-0.072}$ $0.287^{+0.02}_{-0.02}$	$0.483^{+0.025}_{-0.025}$	$0.572^{+0.03}_{-0.03}$	$0.65^{+0.11}_{-0.11}$	$0.73^{+0.12}_{-0.12}$	Gibson et al. (2010); Zhou et al. (2014); Anderson et al. (2013)
WASP-24b		$0.159^{+0.013}_{-0.013}$	$0.202^{+0.018}_{-0.018}$			Smith et al. (2012b)
WASP-33b	$0.27^{+0.04}_{-0.04}$ $0.244^{+0.027}_{-0.02}$	$0.26^{+0.05}_{-0.05}$	$0.41^{+0.02}_{-0.02}$			Deming et al. (2012); de Mooij et al. (2013)
WASP-36b	$0.13^{+0.04}_{-0.04}$					This Work
WASP-43b	$0.194^{+0.029}_{-0.029}$ $0.197^{+0.042}_{-0.042}$ $0.181^{+0.027}_{-0.027}$	$0.347^{+0.013}_{-0.013}$	$0.382^{+0.015}_{-0.015}$			Wang et al. (2013); Chen et al. (2014a); Zhou et al. (2014); Blecic et al. (2014)
WASP-46b	$0.253^{+0.063}_{-0.06}$ $0.26^{+0.04}_{-0.04}$					Chen et al. (2014c); This Work

Table A1 – *continued*

Planet	*Ks* depth (%)	[3.6] depth (%)	[4.5] depth (%)	[5.8] depth (%)	[8.0] depth (%)	References
WASP-48b	$0.109^{+0.027}_{-0.027}$	$0.176^{+0.013}_{-0.013}$	$0.214^{+0.02}_{-0.02}$			O'Rourke et al. (2014)
WASP-76b	<0.3					This Work
WASP-80b		$0.0455^{+0.01}_{-0.01}$	$0.0944^{+0.0064}_{-0.0065}$			Triaud et al. (2015)
XO-1b		$0.086^{+0.007}_{-0.007}$	$0.122^{+0.009}_{-0.009}$	$0.261^{+0.031}_{-0.031}$	$0.21^{+0.029}_{-0.029}$	Machalek et al. (2008)
XO-2b		$0.081^{+0.017}_{-0.017}$	$0.098^{+0.02}_{-0.02}$	$0.167^{+0.036}_{-0.036}$	$0.133^{+0.049}_{-0.049}$	Machalek et al. (2009)
XO-3b		$0.101^{+0.004}_{-0.004}$	$0.143^{+0.006}_{-0.006}$	$0.134^{+0.049}_{-0.049}$	$0.15^{+0.036}_{-0.036}$	Machalek et al. (2010)
XO-4b		$0.056^{+0.012}_{-0.006}$	$0.135^{+0.01}_{-0.007}$			Todorov et al. (2012)

This paper has been typeset from a TEX/LATEX file prepared by the author.